

Worcester Polytechnic Institute Digital WPI

Masters Theses (All Theses, All Years)

Electronic Theses and Dissertations

2004-04-30

Development of a Monte Carlo Simulation Method for use in investigating CT (Computed Tomography) Mammography

Samta C. Thacker

Worcester Polytechnic Institute

Follow this and additional works at: <https://digitalcommons.wpi.edu/etd-theses>

Repository Citation

Thacker, Samta C., "Development of a Monte Carlo Simulation Method for use in investigating CT (Computed Tomography) Mammography" (2004). *Masters Theses (All Theses, All Years)*. 569.
<https://digitalcommons.wpi.edu/etd-theses/569>

This thesis is brought to you for free and open access by Digital WPI. It has been accepted for inclusion in Masters Theses (All Theses, All Years) by an authorized administrator of Digital WPI. For more information, please contact wpi-etd@wpi.edu.

**DEVELOPMENT OF A MONTE CARLO SIMULATION METHOD FOR USE IN
INVESTIGATING CT (COMPUTED TOMOGRAPHY) MAMMOGRAPHY**

by

Samta C. Thacker

A Thesis

Submitted to the Faculty

of the

WORCESTER POLYTECHNIC INSTITUTE

in partial fulfillment of the requirements for the

Degree of Master of Science

in

Biomedical Engineering

May 2004

APPROVED:

Dr. Stephen J. Glick, PhD., Research Advisor

Dr. Christopher H. Sotak, PhD., Thesis Committee

Dr. Ross D. Shonat, PhD., Thesis Committee

ABSTRACT

The development of new digital mammography techniques such as dual-energy imaging, tomosynthesis and CT mammography will require investigation of optimal camera design parameters and optimal imaging acquisition parameters. One tool that is useful for this purpose is Monte Carlo simulation. This study presents a methodology for generating simulated images from a CsI-based, flat-panel imager model and for estimating the normalized glandular dose to the uncompressed breast in CT mammography. The simulation uses the GEANT 3 Monte Carlo code to model x-ray transport and absorption within the CsI scintillator, and the DETECT-II code to track optical photon spread within a columnar model of the CsI scintillator. The Monte Carlo modeling of x-ray transport and absorption within the CsI was validated by comparing to previously published values for the probability of a K-shell interaction, the fluorescent yield, the probability of a K-fluorescent emission, and the escape fraction describing the probability of a K x-ray escaping the scintillator. To validate the combined (GEANT 3 coupled with DETECT-II) Monte Carlo approach to form simulated images, comparison of modulation transfer functions (MTFs) and system sensitivity (electrons/mR/pixel) obtained from simulations were compared to empirical measurements obtained with different x-ray spectra and imagers with varying CsI thicknesses. By varying the absorption and reflective properties of the columnar CsI used in the DETECT-II code, good agreement between simulated MTFs and system sensitivity and empirically measured values were observed. The Monte Carlo software was also validated for dosimetry by comparing results of the linear

attenuation coefficient values and the normalized glandular dose (DgN) values of the compressed breast, to those reported in the literature. The normalized glandular dose was then estimated for three different sizes of the uncompressed breast with a homogeneous composition of adipose and glandular tissue. Further, fit equations of the normalized glandular dose curves were also generated using MATLAB. These equations can be used to replicate the dose for the three sizes of the breast and three compositions of the adipose and glandular tissue. In addition, images displaying energy deposition maps are presented to better understand the spatial distribution of dose in CT mammography.

ACKNOWLEDGEMENTS

I would like to thank everyone who was involved directly or indirectly in the completion of my thesis. I would like thank my research advisor Dr. Stephen Glick for providing me with an opportunity to work under him. His continuous guidance helped me in understanding the physics involved in CT mammography. I would also like to thank my committee members Dr. Christopher Sotak and Dr. Ross Shonat for their invaluable help and patience throughout my M.S. program. I would like to extent my gratitude to Dr. Aldo Badano (FDA) for his valuable suggestions and guidance. I would like to thank my research laboratory members Aruna Vedula, Corinne Groiselle, Stefaan Vandenberghe and Xing Gong for their continuous help. I would like also like to thank Ina Lemon and Jean Seiquet for their help whenever I needed. Finally, I would like thank my parents and my family for their continuous love and support throughout my M.S. program. This project was supported by Grant Number CA-92191 from the National Institute of Health (NIH).

TABLE OF CONTENTS

Abstract	ii
Acknowledgements	iv
List of figures and tables	vi
List of Appendices	viii
Chapter 1. Introduction.....	1
Chapter 2. Background.....	5
Chapter 3. Specific Aims	13
Chapter 4. Materials and Methods	14
Chapter 5. Results and Discussion.....	30
Chapter 6. Conclusion	43
References.....	45
Appendices.....	49

LIST OF FIGURES AND TABLES

Figures	Page
Figure 1: Anatomy of the breast.....	1
Figure 2: Film-Screen and Digital Mammography	2
Figure 3: Image acquisition process.....	7
Figure 4: Generation of Characteristic radiations and Auger electrons.....	8
Figure 5: Proposed CT geometry.....	11
Figure 6: CsI scintillator modeled in DETECT-II.	14
Figure 7: (A) Generation of Line Spread Functions. (B) Examples of Line Spread Functions and Optical Collection Efficiencies computed from DETECT-II.	15
Figure 8: 30 - 140 kVp Tungsten-anode spectra.	18
Figure 9: Flowchart describing the process of simulation of images.	19
Figure 10: Geometry for computing linear attenuation coefficient.	22
Figure 11: Geometry for computing DgN coefficients for compressed breast.	23
Figure 12: Compressed and uncompressed breast volumes.	26
Figure 13: Geometry for computing DgN coefficients for uncompressed breast.	28
Figure 14: Probability of K x-rays reabsorption vs. thickness.	31
Figure 15: Energy distribution along the depth of CsI scintillator.	32
Figure 16: Pre-sampling MTF for 100 μ CsI scintillator.....	33
Figure 17: Scintillator MTF for 300 μ CsI scintillator.	34

Figure 18: Comparison with linear attenuation coefficients in the literature.	35
Figure 19: Graph shows a comparison of the DgN values published by Boone along the y-axis with the Monte Carlo derived DgN values in the present study along the x-axis. The data are shown for 100% glandular compressed breast phantom having a breast thickness of 10cm, 6cm and 2 cm and an excellent correlation is observed.	36
Figure 20: The monoenergetic DgN values computed from Monte Carlo simulations corresponding to three breast compositions of 5% glandular, 50% glandular and 100% glandular respectively are shown in the panels [(A), (B) and (C)] respectively. The data are shown for the three different sizes of the uncompressed breast.	37
Figure 21: The effect of change in skin thickness (from 4mm to 2mm) on DgN values. As seen from the graph, no significant difference was observed over all the energies.	39
Figure 22: Graph shows a comparison of the DgN values over all the energies of the medium-sized cylindrical breast phantom with the DgN values of the hemi-ellipsoid phantom having a 50% glandular breast tissue composition. The DgN values for the hemi-ellipsoid are higher over all the energies but not a significant difference is observed.	40
Figure 23: The images of the distribution of the energy deposited in the cylindrical breast phantom having incident energy of 20 keV, 40 keV, 60 keV and 80 keV are shown in panels (a), (b), (c) and (d), respectively. The panels (e), (f), (g) and (h) show the profiles of the fractional energy deposited in the breast versus the depth through the breast.	40

Tables

Table 1: Comparison with K-fluorescence characteristics in the literature.	30
Table 2: Area under each of curve of the distribution of the energy along the depth of CsI scintillator.	32

LIST OF APPENDICES

Appendices	Page
Appendix A: Fit-equation for small-sized breast model	49
Appendix B: Fit-equation for medium-sized breast model	50
Appendix C: Fit-equation for large-sized breast model	51
Appendix D: Operating procedure for GEANT simulation	52
Appendix E: Operating procedure for DETECT-II simulation.....	73

Chapter 1

INTRODUCTION

Breast cancer is the uncontrolled growth of epithelial glandular cells. The anatomy of the breast is shown in Figure 1. Mammography is the best-known method for early detection of breast carcinoma and is known to reduce breast cancer mortality by approximately 25-30% [1]. Breast cancer is detected on the basis of four types of signs on the mammogram [2]:

- a. the characteristic morphology of a tumor mass.
- b. certain presentations of mineral deposits as specks called microcalcifications.
- c. architectural distortion of normal tissue patterns caused by the disease.
- d. asymmetry between corresponding regions of images of the left and right breast.

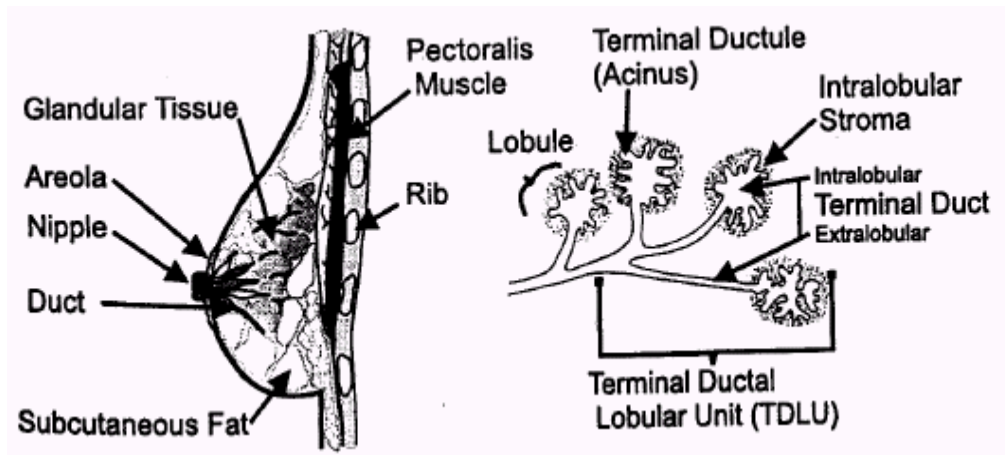


Figure 1: Anatomy of the breast.[2]
Handbook of medical imaging, vol. 1, Physics and Psychophysics.

Methods for imaging the breast run from standard techniques such as x-ray mammography, to highly experimental ideas, such as confocal microwave imaging. Some of the imaging

technologies for breast cancer include film-screen mammography, which is most routinely used and digital mammography, which is infrequently used as it is expensive and is still unknown to many people. Both these imaging technologies are shown in Figure 2.

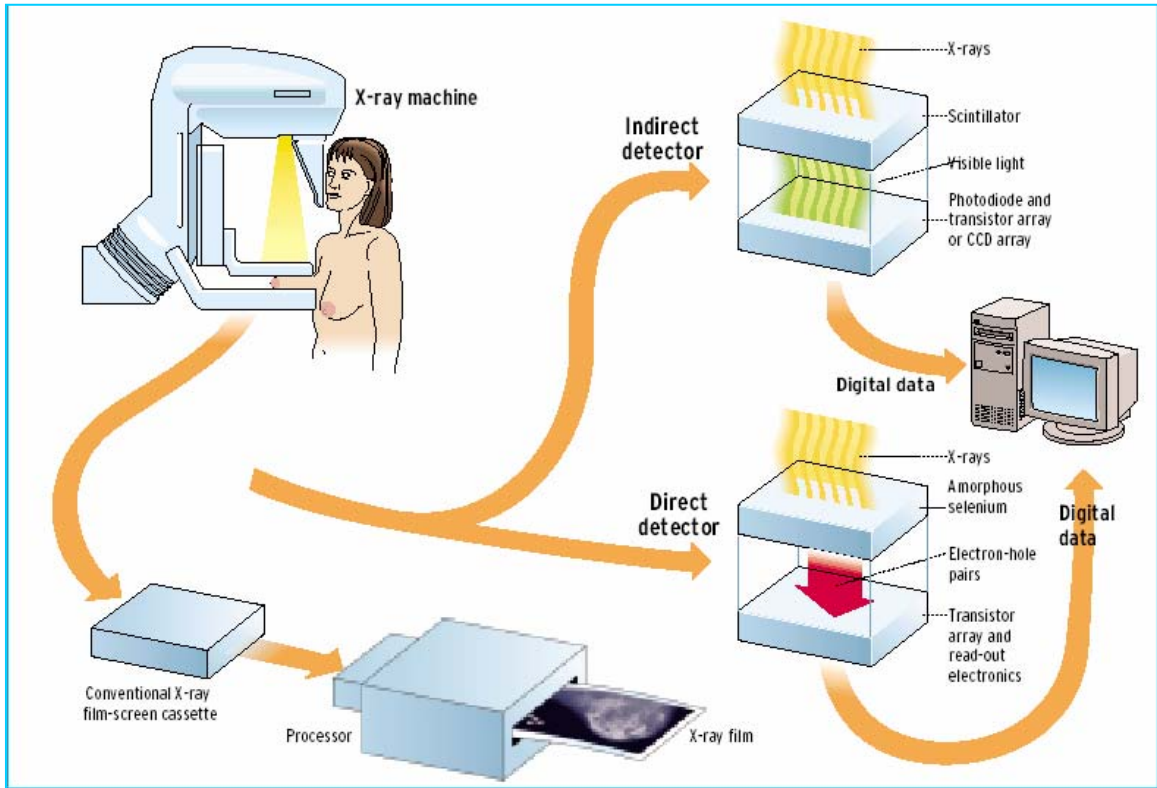


Figure 2: Film-Screen and Digital Mammography. [3]
<http://www.spectrum.ieee.org/WEBONLY/pressrelease/0501/cancer0501.pdf>

In all types of mammography, the x-ray photons are given off by the x-ray source and directed towards the patient. In conventional mammography, the development of a film-screen cartridge produces the mammogram and is shown in Figure 2. In digital mammography, detection can be done in two ways. With indirect detection, x-rays pass through the patient's breast and hit the scintillator. A scintillator is a material that converts x-ray energy into visible light. The scintillator is coupled to a photodetector array or connected to tiles of charge-coupled devices (CCDs) by tapered optical fibers. Needle-

like crystals of cesium iodide (CsI) is typically used as a scintillator. An amorphous silicon detector made up of photodiodes and a thin-film transistor (TFT) is used as the readout circuitry. As illustrated in Figure 2, with direct detection, the original CCD-based indirect system is replaced by an amorphous silicon TFT array coated in amorphous selenium. A voltage is placed across the selenium, and wherever an x-ray strikes it, electron-hole pairs are formed. These pairs are then collected by integrated capacitors associated with the pixel elements of the TFT array, and the image is read out by electronics integrated in the array. [3].

Although film-screen mammography has saved many lives and is considered the imaging modality of choice for early detection of breast cancer, it is far from perfect. Digital mammography provides excellent image quality, and has a number of advantages as compared to film-screen mammography systems. Some of these advantages are the potential to acquire the images faster, to easily store the images; to manipulate the contrast and magnification of the images, and the potential for digital post processing of the acquired images. One of the limiting problems with conventional mammography is that the recorded image represents the superposition of a three-dimensional (3D) object (i.e., the breast) onto a two-dimensional (2D) plane. Thus, even though breast compression is usually done, normal anatomical structure can combine with useful diagnostic information (e.g., a tumor mass) in such a way as to impede visualization and reduce lesion detectability. One technique that can be used to improve 3D visualization of objects is computed tomography or CT.

One of the major goals of this project was to develop a module for the GEANT 3 Monte Carlo simulation [4] to model digital mammography using an indirect flat-panel imager with a structured CsI scintillator. The spread of optical photons through the CsI was modeled by incorporating results based on an optical DETECT-II Monte Carlo simulation [5] developed by our collaborator, Dr. Aldo Badano at the U.S. Food and Drug Administration. Simulated projection data can then be used to optimize CT mammography system design, as well as to evaluate reconstruction methods. Another major goal of this project was to use the Monte Carlo simulation to compute the normalized glandular dose to the uncompressed breast in CT geometry. Knowledge of the radiation dose to the uncompressed breast is important for optimizing and evaluating proposed CT mammography system.

A brief overview of the two Monte Carlo tools, GEANT and DETECT-II, are included in the appendices D and E, respectively.

Chapter 2

BACKGROUND

Development of new digital mammography techniques such as dual-energy imaging, tomosynthesis and CT mammography often requires an analysis to determine optimal camera design parameters and imaging techniques. Some of these design parameters include pixel size, thickness of the x-ray converter, imaging geometry (i.e., magnification), kVp setting, spectrum shape, and scatter grid. In order to determine these optimal parameters, a figure-of-merit (FOM) is needed. The most commonly used FOMs for system design optimization are the detective quantum efficiency (DQE) and the noise equivalent quanta (NEQ). These FOMs are computed from the modulation transfer function (MTF) and the noise power spectrum (NPS).

Modulation Transfer Function:

The modulation transfer function (MTF) of an imaging system describes the spatial-response properties of the system. The MTF is defined as the amplitude of the Fourier transform of the point spread function (PSF) of the system, which is the response of the system to a delta-function. Thus, MTF can be defined as,

$$MTF(u, v) = |OTF(u, v)|, \quad (1)$$

where $OTF(u, v)$ is the optical transfer function, the Fourier transform of the PSF.

The pre-sampled MTF is the system response excluding the stage of pixel sampling.

Detective Quantum Efficiency:

The performance of an image detector is well characterized by its detective quantum efficiency, $DQE(u, v)$, which describes the transfer of signal-to-noise from the input to the output of the imager as a function of spatial frequency [6].

$$DQE(0) = A_S \times A_Q, \quad (2)$$

where $DQE(0)$ is the detective quantum efficiency at zero frequency, A_S is the Swank Factor and A_Q is the scintillator efficiency.

Since these FOMs do not take into account the diagnostic task, for example, what the image is used for, a number of researchers have investigated [7] task-based performance measures such as the ideal observer signal to noise ratio (SNR). To compute these task-based FOMs, knowledge of how the signal and noise is transferred through the detector system is typically required.

Figure 3 illustrates the stages of signal and noise transport in an indirect detector model. In Figure 3, x-rays of varying energy are incident on the detector. The incoming x-ray after passing through the object interacts within the scintillator. A cesium iodide (CsI) scintillator is modeled here. This interaction process can be modeled as a binomial selection process that produces noise in the detector. If the incoming photon has energy greater than the binding energy of the K-shell of cesium or iodine, it is capable of producing a K x-ray which may escape out or be reabsorbed in the scintillator.

Depending on the energy deposited from this interaction, the energy gets converted to optical photons. This conversion to optical photons can be modeled as a Poisson process with the variance on the number of optical photons emitted equal to the mean number emitted. Thus, this energy to light conversion process introduces more noise. These optical photons get scattered in the scintillator as they travel towards the detector, and are finally collected by the pixelized detector. The scattering of the optical quanta can be modeled as a Poisson process and the collection of the optical quanta can be modeled as a binomial selection process. Both these processes contribute to noise in the recorded image.

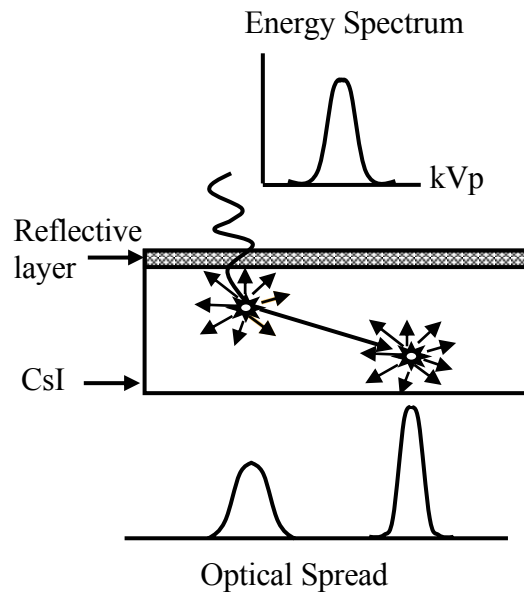


Figure 3: Image acquisition process.

A generalized approach to describing noise-power transfer through medical imaging systems has been developed over the past several years in which image-forming processes are represented in terms of a cascade of amplified point processes [8]. Two theoretical

models that have been described are the serial-cascade model [9] and the parallel-cascade model [8, 10]. The parallel cascade model incorporates the effects of characteristic x-ray reabsorption. There are a number of detector parameters that are needed to implement these cascade models.

The parameters that need to be estimated to evaluate performance using the above mentioned models are the characteristics of the x-ray interactions and the light spread. Some of these parameters are the probability of producing a characteristic K-shell x-ray ($\zeta(\omega)$), the probability of a K-shell x-ray being reabsorbed (f_k), the point spread function (PSF) of K-shell x-ray reabsorption (T_k), the PSF of optical spread of the light photons, and the optical collection efficiency for different depths.

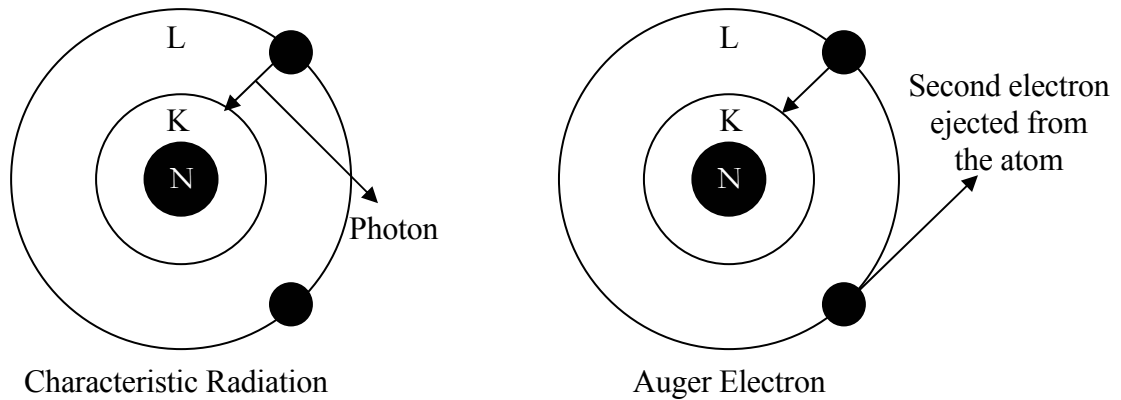


Figure 4: Generation of Characteristic radiations and Auger electrons.

Figure 4 illustrates the process of formation of a characteristic radiation or an Auger electron. If the incident photon has energy greater than the binding energy of the K-shell of cesium or iodine, it is capable of knocking-off the electron from that shell. This electron will have energy equal to the difference between the incoming photon energy and the K-

shell binding energy. Thus, a hole is created in this shell which may be filled by an electron from the outer shells (either L, M). The difference in the energy between the outer shell and the K-shell is given out as “Characteristic Radiation” also known as “K x-ray”.

Following the ionization of the atom by the incident photon and the falling back of outer shell electron to fill the inner shell vacancy, an alternative method of releasing the energy is through the ejection of another outer shell electron, thus leaving the atom doubly ionized. This electron is called the “Auger Electron”.

Some of these parameters cannot be measured experimentally. Therefore, one tool that is useful for this purpose is Monte Carlo simulation.

The Monte Carlo method is widely used for solving problems involving statistical processes and is very useful in medical physics due to the stochastic nature of the radiation emission, transport and detection processes. In a Monte Carlo simulation, each of the millions of photons traced in computations undergoes absorption or scattering, depending on the outcome of a random number generator.

One part of this project describes a computer simulation approach for modeling a CsI-based a:Si flat-panel detector to obtain parameters needed in computing FOMs for volumetric breast imaging systems as well as for generating simulated images from a flat-panel imager. Two Monte Carlo tools were used in the computer simulation the first being the GEANT 3 Monte Carlo code [4] to model x-ray photon transport and absorption within

the CsI scintillator, and the second being DETECT-II [5] to model optical photon spread within the columnar CsI scintillator.

The simulation is validated by comparing results to previous publications, as well as to experimental measurements.

Another design parameter that is important for performing imaging system optimization for innovative breast imaging approaches is the radiation dose given to the breast. The determination of breast dosimetry for mammographic techniques is also important for evaluating carcinogenic risk. Since the glandular tissue of the breast is believed to be the most radio-sensitive of the tissues composing the breast, national radiation protection councils currently recommend that the mean dose to the glandular tissue be used as a dosimetric quantity to predict radiation risk associated with mammographic procedures. Previous studies [11] have used Monte Carlo simulations to compute normalized glandular dose (DgN) values (mean glandular dose per unit entrance surface exposure) as a function of x-ray beam quality, x-ray tube target/filter material, breast thickness, and breast composition. Given the DgN coefficients as a function of energy for a specified breast composition, and the relative x-ray spectra incident on the breast surface, the mean glandular dose (MGD) can be computed.

Recently, volumetric cone-beam CT mammography using a digital flat-panel detector has been proposed [12]. Figure 5 illustrates the proposed geometry of such an imaging system. In this system, the patient would lie in the prone position on a table with a cut-out in which the breast would hang in the pendant position. Some type of support for the breast

would be used to minimize patient motion, which might include slight compression of the breast upwards towards the chest wall (applied to the nipple). The x-ray tube and detector would rotate around the breast and two-dimensional (2D) projections would be collected over many views using half cone-beam geometry. These projections would then be reconstructed to provide a three-dimensional (3D) representation of the breast.

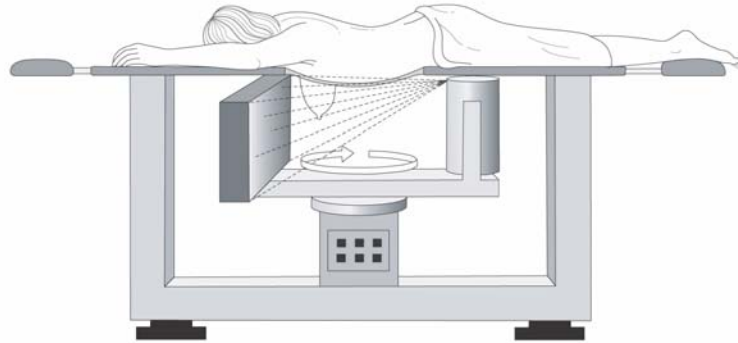


Figure 5: Proposed CT geometry.

Studies have been conducted to optimize flat-panel CT mammography system parameters such as acquisition geometry, kVp setting, detector pixel size, and scintillator thickness; however, a critical parameter required for accurate optimizations is the MGD for a particular acquisition protocol. Since the literature is rich with reports of dosimetry data for mammography using a compressed breast model, one approach that has been used to explore flat-panel CT mammography is to assume that the MGD to the uncompressed pendant breast is similar to that of the compressed breast with thickness equal to the

diameter of the uncompressed breast. The problem with this assumption is that the shapes of the compressed and uncompressed breast are different which could result in different dosimetry. Boone et al [13] have recently studied breast dosimetry for the uncompressed pendant breast; however, they model more traditional fan-beam CT acquisition geometry.

Another part of this project describes a computer simulation approach for computing DgN coefficients as a function of energy for the uncompressed pendant breast using the proposed flat panel CT mammography geometry shown in Figure 5. GEANT 3 Monte Carlo code [4] was used in the computer simulation to model x-ray photon transport and absorption within the breast phantom and the CsI scintillator. The simulation is validated by comparing results of DgN coefficients for the compressed breast model to previous publications.

Chapter 3

SPECIFIC AIMS

1. To develop a detector module that modeled a CsI scintillator. The GEANT 3 Monte Carlo program was used to track x-ray transport through the breast phantom and into the CsI phosphor. Optical photon spread was modeled using point-spread functions (PSFs) computed from DETECT-II Monte Carlo program. The GEANT 3 simulation will output x, y, z coordinates (spatial coordinates, depth) and energy for each particle absorbed in the CsI. The contribution to the image from this interaction in the phosphor was computed by integrating the appropriate PSF over the 2D pixelized detector, and scaling using the appropriate optical collection efficiency. By repeating this convolution blurring at each step for each particle interaction, the resulting projection image can be formed.
2. To verify the accuracy of the Monte Carlo simulation, physical characteristics measured using the simulated detector was compared to previous empirical measurements reported in the literature, as well as to those measured at UMASS using a similar digital mammography detector. These include fluorescent yield, escape fraction, K-fluorescence emission, PSF of energy absorbed, and the pre-sampling modulation transfer function (psMTF). The differences between simulated and measured data were explored.
3. One of the desired constraints in CT mammography is that the mean glandular dose (MGD) be equivalent (or nearly equivalent) to a typical two-view diagnostic mammography study. Thus, it is imperative to understand the radiation dose given to the uncompressed breast using the proposed CT geometry. This part of the thesis involved replicating previous dosimetry data for the compressed breast published in the literature, and then moved on to investigating dosimetry of the breast for CT mammography.

Chapter 4

MATERIALS AND METHODS

The computer simulation uses two publicly available Monte Carlo codes, GEANT 3 and DETECT-II for modeling a CsI-based a:Si flat panel detector and to estimate the radiation dose to the breast in CT geometry.

GEANT 3 is a general purpose Monte Carlo code used to track x-ray transport. The software was set up to model monochromatic x-ray emission from a "point-like" x-ray tube. It was also set up to model photoelectric effect, Compton and Rayleigh interactions.

DETECT-II models optical photon transport. The software was modified to model structured (columnar) CsI [5] as shown in Figure 6.

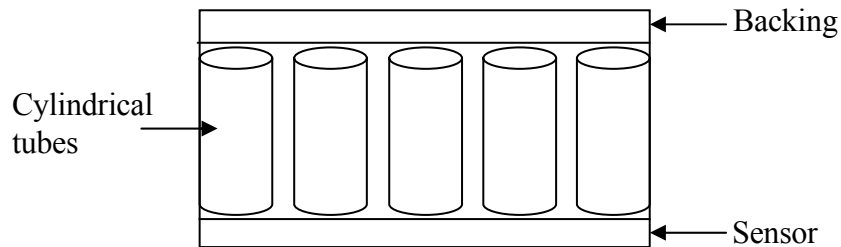


Figure 6: CsI scintillator modeled in DETECT-II.

Inputs to the DETECT-II code include the diameter of the cylindrical tubes, reflectivity of the backing and the sensor, and absorption and scattering coefficients. By placing an isotropic emitting light source at the center of the tube at each varying depths, we can

compute depth-dependent optical line spread functions (LSFs) and optical collection efficiencies (OCEs) (see Figure 7A).

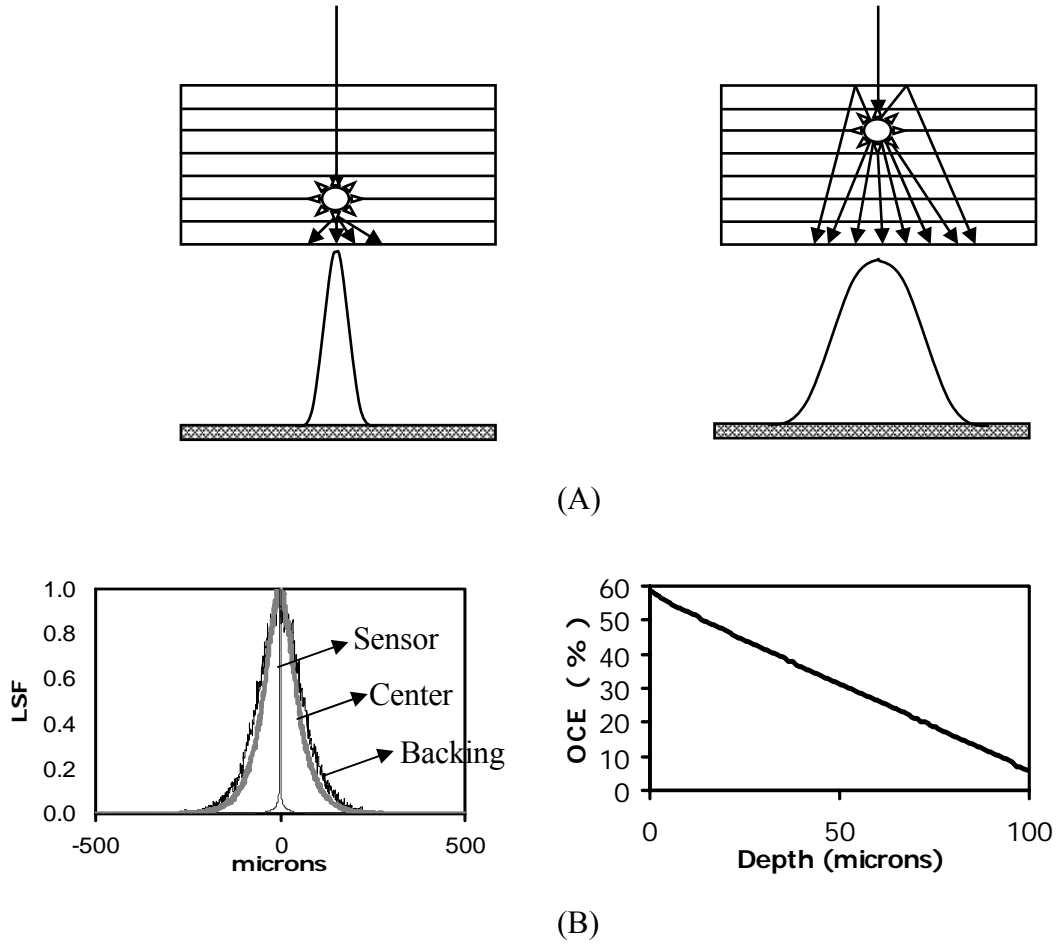


Figure 7: (A) Generation of Line Spread Functions. (B) Examples of Line Spread Functions and Optical Collection Efficiencies computed from DETECT-II.

Figure 7B shows an example of the line spread functions and the optical collection efficiencies computed from DETECT-II. In this case, the LSFs were generated by placing a light source at three different depths in a 100 μm thick CsI scintillator. The narrow curve

shows the LSF measured for the light source near the sensor, the wide curve shows the LSF measured for the light source near the entrance (backing), and the middle curve shows the LSF measured for the light source near the center of the 100 μm CsI scintillator. The OCE vs. depth curve (Figure 7B) shows that approximately 60% of the optical photons generated in the depth closest to the sensor are collected; whereas, approximately only 5% are collected from a depth very far away from the sensor.

4.1 Computer simulation for modeling a CsI-based a:Si flat panel detector

Investigation of the x-ray interactions was done by comparing computed physical parameters computed using GEANT 3 to published values. Figures displaying energy deposition curves are presented to better understand the distribution of energy along the depth of the CsI scintillator.

4.1.1 Computation of physical parameters

Tungsten anode spectra [15] simulated in a pencil beam was directed towards varying thicknesses of CsI scintillator. Photoelectric, Compton, and Rayleigh interactions within the CsI were modeled. If the incoming photon interacts with the K-shell, it can either produce Characteristic Radiation or an Auger Electron.

From the known energy levels of the characteristic radiations and Auger electrons, the number of characteristic radiations and Auger electrons produced were computed. From these values, the following parameters were computed; 1) probability of a K-shell interaction, 2) fluorescent yield, 3) probability of a K-fluorescence emission, and 4) escape

fraction, by using the following equations. Results of these computations were compared to previously reported values [16, 17].

$\text{Probability of K-Shell interaction} = \frac{\# \text{ of K x-rays produced} + \# \text{ of Auger electrons produced}}{\# \text{ of x-rays absorbed}}$
$\text{Fluorescent Yield} = \frac{\# \text{ of K x-rays produced}}{\# \text{ of K x-rays produced} + \# \text{ of Auger electrons produced}}$
$\text{Escape Fraction} = \frac{\# \text{ of K x-rays escaped}}{\# \text{ of x-rays absorbed}}$
$\text{Probability of K - Fluorescence Emission} = \frac{\# \text{ of K x-rays produced}}{\# \text{ of x-rays absorbed}}$

4.1.2 Computation of the distribution of energy along the depth of CsI

Tungsten anode spectra shown in Figure 8 [15] simulated in a pencil beam was directed towards a 380 μ thick CsI scintillator. Photoelectric, Compton, and Rayleigh interactions within the CsI were modeled. A total of 1 million photons were simulated for each kVp value. The depth of the CsI scintillator (380 μ) was divided into 19 bins of 20 microns each. At the site of each energy deposited event, the corresponding bin was computed from the depth (Z- co-ordinate) and the energy deposited at that location was cumulatively added into that bin. The energy in each bin was finally divided by the total incident energy to compute the fractional energy from equation (3),

$$\text{Fractional Energy} = \frac{\text{Energy deposited}}{\text{Total incident energy}}, \quad (3)$$

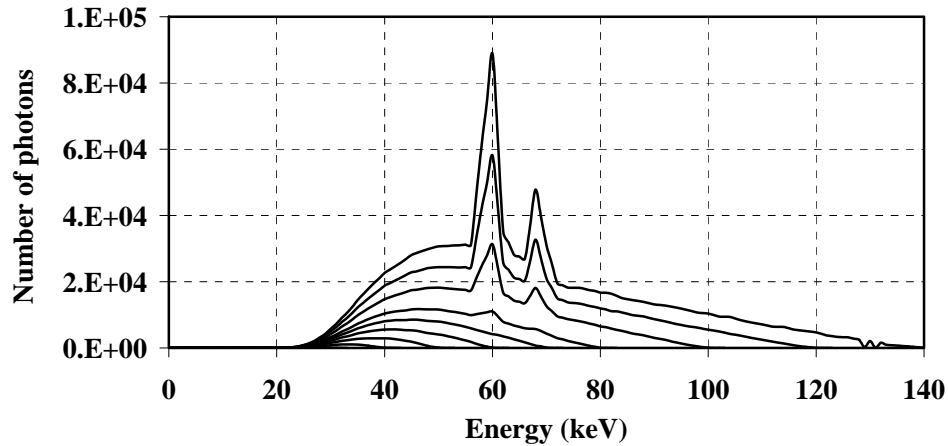


Figure 8: 30 - 140 kVp Tungsten-anode spectra.

4.1.3 Process of simulation of images

Figure 9 describes the simulation process. To simulate optical photon transport through the CsI, DETECT-II was used to form a lookup table of pre-computed optical point spread functions (PSFs) and optical collection efficiencies (OCEs) as a function of depth in the columnar CsI scintillator. GEANT 3 was used to follow x-ray transport within the CsI and to output the x, y, z coordinates (spatial coordinates and depth) and energy of all absorbed x-rays. Depending on the z-location (depth), the corresponding OCE for that depth and the energy absorbed at that location were used to form a probability density function (PDF) with a mean equal to $58 \times OCE(z) \times E$. Holl et al. [18] measured that 52,000 optical photons were emitted per 1-MeV absorbed and Jing et al. [19, 20] reported that 64,000 optical photons were emitted per 1-MeV absorbed. Hence, we assumed that 58 optical photons were emitted per keV absorbed, a mean value between the two reported values. We assume the PDF to have a Poisson distribution with variance equal to the mean. A random

deviate was selected from this PDF using a random number generator. The contribution to the image from each absorbed x-ray was then computed by integrating the appropriate optical PSF (for that depth) over the pixelized detector and scaling using the random conversion gain.

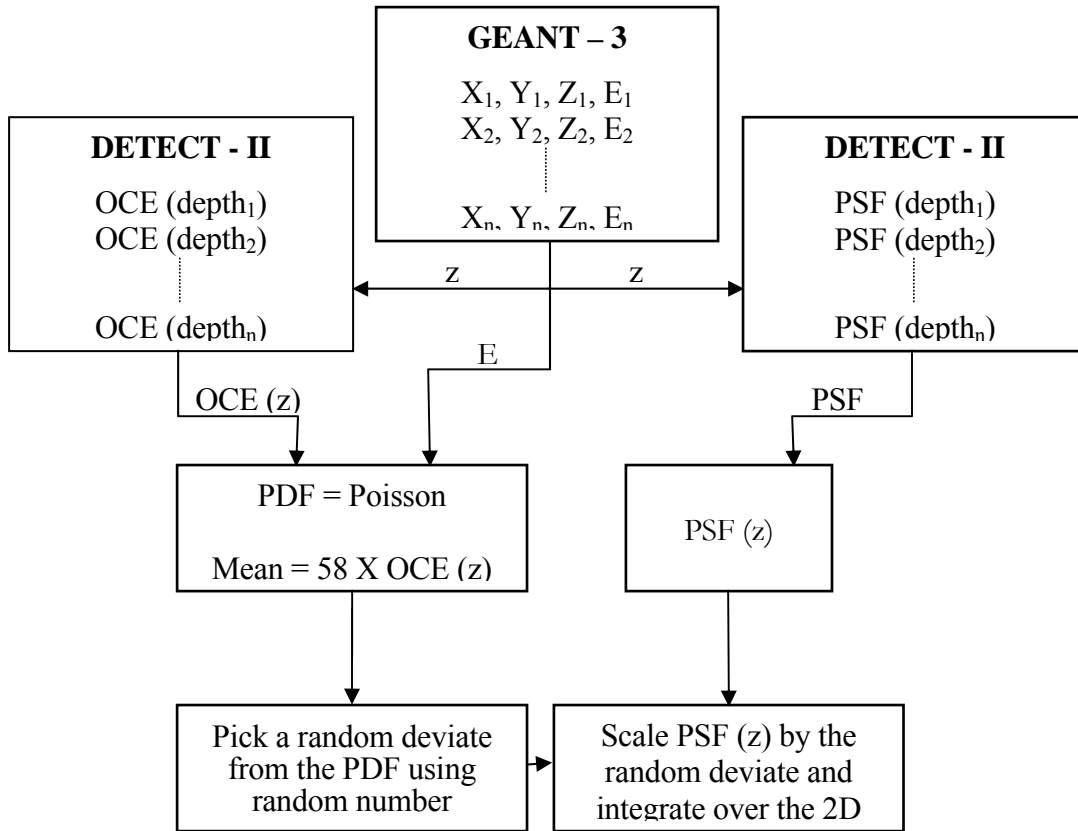


Figure 9: Flowchart describing the process of simulation of images.

4.1.4 Validation of the simulation

The simulation is validated by comparing results of Modulation Transfer Function (MTF), and sensitivity of the flat-panel to previous publications, as well as to experimental measurements.

Using the same approach used for simulation of images, MTFs for varying x-ray spectra were generated by simulating a narrow beam of x-rays that was incident on the detector. The number of x-rays simulated at each energy was specified by the desired x-ray spectra. An absorption coefficient of 1.0 cm^{-1} , scattering coefficient of 600 cm^{-1} , backing reflectivity of 5% and a sensor reflectivity of 10% were chosen as inputs in DETECT-II for the generation of the MTFs. These DETECT-II parameters were chosen on a trial and error basis by starting with values reported in the literature [21, 22] and were chosen solely on the criterion of providing a good match to the MTFs. The pre-sampling MTF (psMTF) was computed by modeling the GE prototype digital mammography imager with 100 μm thick CsI, 100 μm pixel size, and using a 28 kVp, Mo/Mo x-ray spectra and compared to the measured psMTF of a GE prototype digital mammography system as reported by Vedantham et al. [23].

In volumetric breast imaging, a higher energy spectrum will be required [24], so a scintillator MTF was computed using a higher energy 72 kVp, W/Al x-ray spectra and a thicker CsI scintillator of 300 μm . This higher energy MTF was compared to measurements reported by Vedantham et al. [25] for the same CsI thickness and energy spectra. In addition, system sensitivity was computed by using the same geometry and by assuming that 58 optical photons per keV are emitted. A fill-factor of 75% was also assumed. Sensitivity was computed for a 100 μm thick CsI scintillator by using a 28 kVp Mo/Mo spectra hardened by 4.5 cm of Lucite. With the assumption that one optical photon incident on the pixelized a:Si detector created one electron, the number of electrons per mR per 100 μm pixel were computed and converted to digital units per mR per 100 μm pixel

(DU/mR/pixel). This computed sensitivity was then compared to the measured sensitivity of the GE prototype digital mammography system reported by Vedantham et al. [23].

4.2 Computer simulation of breast dosimetry

The GEANT 3 Monte Carlo software was also used for this study. The software was set up to model monochromatic x-ray emission from a "point-like" x-ray tube and then to follow x-ray transport within the breast, modeling photoelectric, Compton and Rayleigh scattering interactions. Elemental compositions of adipose tissue, glandular tissue and skin as reported by Hammerstein [26] were used. The energy deposition in the skin and breast compartments was recorded for use in computing the DgN coefficients. As suggested by Wilkinson and Heggie [27], the energy deposited within the glandular tissue was computed by weighting all energy depositing events within the breast compartment by the energy dependent ratio of the mass energy absorption coefficient of glandular tissue to the mass energy absorption coefficient of the combined adipose/glandular tissue.

4.2.1. Validation of the simulation

To validate the GEANT 3 Monte Carlo code for dosimetry, linear attenuation coefficient (μ) values of 0% glandular (adipose), 50% glandular and 50% adipose, and 100% glandular compositions were computed from GEANT and compared with those reported in the literature [26, 28]. For validation, normalized glandular dose, DgN coefficients, for conventional mammography using a compressed breast model were also computed and compared to previously published studies [11].

4.2.1.1 Linear Attenuation Coefficients (μ)

The geometry for the computation of the linear attenuation coefficients is shown in the Figure 10. A pencil beam of one million x-rays (N_0) was incident on a 5cm cube (x) with the desired tissue composition. The number of x-rays traversing the cube was computed (N). From these values, the linear attenuation coefficient values (μ) were computed at 5 different energy levels using the equation (4),

$$N = N_0 \times e^{-\mu x}, \quad (4)$$

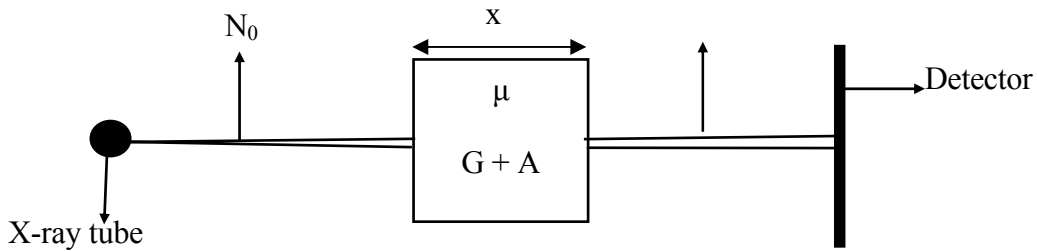


Figure 10: Geometry for computing linear attenuation coefficient.

4.2.1.2 Normalized Glandular Dose (DgN)

To allow for direct comparison to previous studies, DgN coefficients were expressed in the units of mRad per Roentgen. The geometry for these validation studies is identical to that reported by Boone [11] and is shown in Figure 11.

A cylindrical breast shape was used, with the x-ray beam collimated so as to only expose half of the cylinder (i.e., a D-shaped semi-circle) in the cranial-caudal (CC) projection view. The other half of the cylinder acts as backscatter compartment to roughly

model the torso of the patient. The radius of the cylindrical breast model was 8 cm which included a 4 mm skin layer. The source-to-detector distance (SID) was 65 cm. DgN coefficients for x-ray energies ranging from 10-120 keV were computed for breast thicknesses of 2 cm, 6 cm and 10 cm, using homogeneous breast composition of 100% glandular tissue.

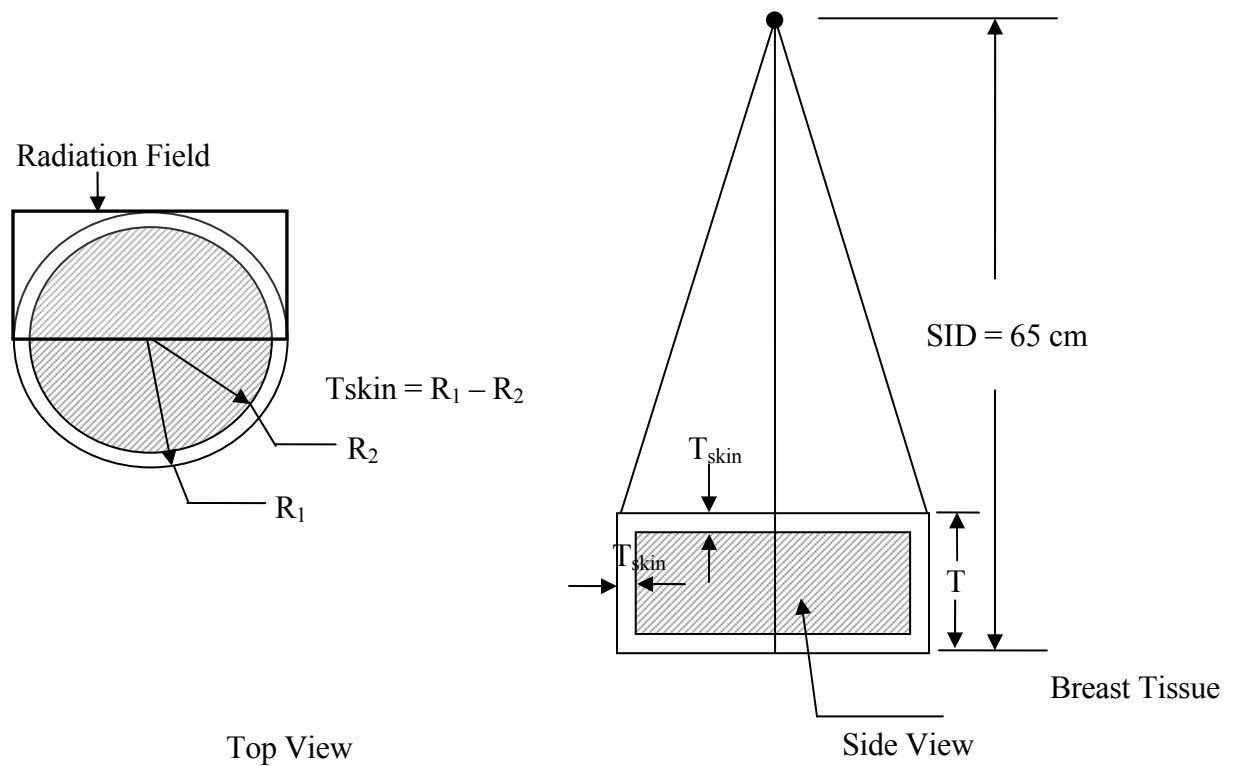


Figure 11: Geometry for computing DgN coefficients for compressed breast.

As pointed out by Boone [11], knowledge of the DgN coefficients, as well as an un-normalized x-ray spectra $I_o(E)$ given in units of photons/mm² is sufficient to compute the MGD.

The MGD is computed using the equation (5),

$$MGD = \frac{\sum_E I_0(E) \times \Phi(E) \times DgN(E)}{\sum_E I_0(E) \times \Phi(E)}, \quad (5)$$

where $\Phi(E)$ is the photon fluence to exposure conversion factor (mR per photons per mm^2).

DgN coefficients were computed using equation (6),

$$D_{gN} = \frac{E_{dep} \times G \times \Phi(E) \times 1.6021 \times 10^{-8}}{mass \times (photons / \text{mm}^2)}, \quad (6)$$

where E_{dep} is the energy deposited in the breast tissue, G is defined later in equation (7) given by Boone [11], $\Phi(E)$ is the photon fluence to exposure conversion factor (photons per square millimeter per roentgen), the constant 1.6021×10^{-8} is a unit conversion factor having units of $(\text{mRad} \times \text{g}) / \text{keV}$ or (milliRad grams per kiloelectronvolts), *mass* represents the mass of only the glandular portion of the breast tissue as given by equation (8) below, and $photons/\text{mm}^2$ is the number of photons incident on a square millimeter area placed on the surface of each breast phantom. G is defined as,

$$G = \frac{f_g \left(\frac{\mu_{en}}{\rho} \right)_g}{\left[f_g \left(\frac{\mu_{en}}{\rho} \right)_g + (1 - f_g) \left(\frac{\mu_{en}}{\rho} \right)_a \right]}, \quad (7)$$

where f_g is the glandular fraction of the breast tissue and (μ_{en}/ρ) is the mass energy

absorption coefficient and ‘*a*’ and ‘*g*’ are the subscripts for adipose and glandular tissue respectively. Mass is computed using the following expression,

$$mass = f_g \times vol \times \rho, \quad (8)$$

where *vol* is the volume of only the breast tissue and ρ is the density of the breast tissue.

4.2.2 Breast dosimetry for CT geometry

In flat-panel CT mammography, it is expected that some type of x-ray transparent, cylindrical breast holder will be needed to stabilize the pendant breast, as well as to help in separating the breast away from the chest wall [12]. In addition, a slight compression of the nipple upwards might be beneficial for reducing the required x-ray cone-beam angle to reduce artifacts in the cone-beam reconstruction algorithm, and to improve uniformity of the x-ray path through the breast. For these reasons, most of the studies described herein have modeled the pendant breast as cylindrical as shown in Figure 12c; however, a hemi-ellipsoidal breast shape was also investigated for comparison purposes.

To estimate the dimensions of the cylindrical and hemi-ellipsoidal uncompressed breast models, published data [29] reporting mean values of the height, width and thickness of the compressed breast on the craniocaudal (CC) view were used. The mean value of the height (H) reported was 10.8 cm. with a standard deviation of 3.72 cm. The mean value of the width (W) was 20.5 cm. with a standard deviation of 3.5 cm. and the mean value of the compressed thickness (C) was 4.4 cm. with a standard deviation of 1.31 cm. From these reported values, 3 breast sizes, large, medium and small, were simulated;

Large = Mean value + standard deviation.

Medium = Mean value.

Small = Mean value – standard deviation.

These three cylinder sizes were computed from [29]. Recently Boone et al [14] conducted a small-scale trial of 200 women to determine the range of breast diameters that exist in the screening population. This was done by measuring the circumference of the each patient's left breast by the mammographic technologist. The results showed that the mean breast diameter was 14.04 cm. with a standard deviation of 2.16 cm. The large-sized breast simulated in the present study was smaller in diameter than the mean diameter reported in Boone's study.

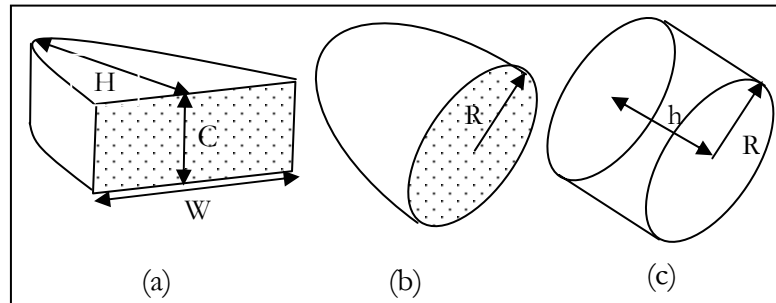


Figure 12: Compressed and uncompressed breast volumes.

Assuming the shaded area for the compressed breast model shown in Figure 12a [29] and the uncompressed breast shown in Figure 12b to be the same, the radius R , and height H , of the uncompressed cylindrical breast model were obtained using the following expressions [29];

$$Volume = 0.785 \times H (cm) \times W (cm) \times C (cm), \quad (9)$$

$$W \times C = \Pi R^2, \quad (10)$$

$$Volume = \Pi R^2 \times h, \quad (11)$$

where *Volume* is the volume of the breast, *W* and *H* is the width and height of the compressed breast on the CC view, *R* is the radius of the uncompressed breast and *h* is the height of the compressed cylinder.

Three cylinders modeling different breast sizes were studied: (1) a small breast, modeled as a cylinder of height 5.5 cm and radius of 4.1 cm; (2) a medium breast modeled as a cylinder of height 8.47 cm and radius of 5.36 cm; and (3) a large breast modeled as a cylinder of height 11.4 cm and radius of 6.6 cm. Each breast phantom was encapsulated by a layer of skin with a thickness of 4 mm. Breast tissue composition was modeled as a homogeneous compound of adipose and glandular tissues.

A hemi-ellipsoid breast shape having the same volume as the medium-sized cylindrical breast phantom with a breast composition of 50% glandular tissue was also investigated for comparison. To investigate the effect of skin thickness, a medium-sized cylindrical breast phantom encapsulated by a layer of skin with a thickness of 2 mm and having a homogeneous breast composition of 50% glandular tissue was also investigated. The skin of the breast is usually 0.5 to 2 mm in thickness [30] and hence a skin layer of 2 mm thickness was also studied. For this phantom, it was assumed that the volume of breast tissue excluding the skin would be the same as that of medium-sized breast phantom with a skin layer of 4 mm. Three breast compositions of 5%, 50% and 100% glandular tissue were studied for each size of the breast model.

The GEANT 3 Monte Carlo code was used to simulate the CT mammography geometry by modeling the x-ray tube as a point source emitting x-rays within a half cone-beam geometry towards the breast model as shown in Figure 13. The central axis of the cone-beam irradiation field (perpendicular to the detector) passed through the breast model, along the top of the breast.

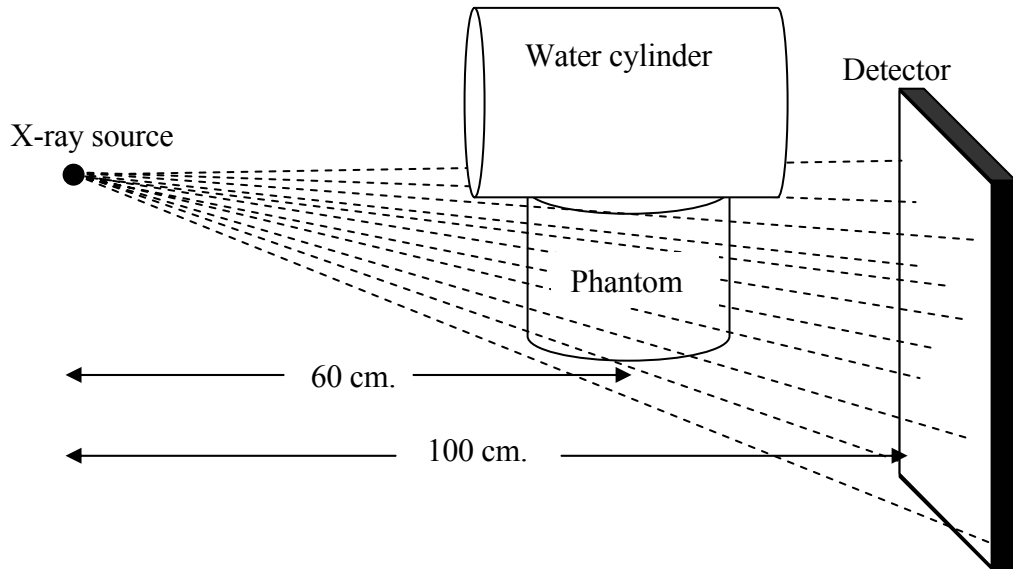


Figure 13: Geometry for computing DgN coefficients for uncompressed breast.

To account for back-scatter from the body, the torso of the patient was modeled using a 30 cm diameter water cylinder positioned on top of the breast model, with its long axis parallel to the central axis of the cone-beam irradiation. A source to image distance (SID) of 100 cm was assumed and the breast phantoms were placed at 60 cm from the x-ray source. For each (monoenergetic) x-ray energy, breast size and breast composition, a simulation run was executed using 1 million entrant x-ray photons. DgN coefficients for x-ray energies ranging from 10-120 keV were computed using surface exposure and absorbed dose for the three breast sizes and compositions. In addition, images displaying energy

deposition maps are presented to better understand the spatial distribution of dose with CT mammography.

Chapter 5

RESULTS AND DISCUSSION

5.1 Computer simulation

A computer simulation was developed to compute the various physical parameters to investigate the x-ray interactions within the CsI scintillator.

5.1.1 Comparison with physical parameters in the literature

Computed values for fluorescent yield, probability of K-shell interaction, probability of a K-fluorescence emission, and escape fraction using the GEANT 3 Monte Carlo code were compared to previously reported values and are shown in Table 1.

Table 1: Comparison with K-fluorescence characteristics in the literature.

	Fluorescent Yield (ω)	Probability of K-shell Interaction (ζ)	Fluorescence Emission ($\zeta\omega$)	Escape Fraction (36 keV)
Cunningham et al; SPIE; 2002	0.89	0.85	0.76	
Hillen et al; SPIE; 1991; (270 μ)	0.885	0.83	0.735	0.318
250 microns	0.87	0.83	0.72	0.32
300 microns	0.87	0.83	0.72	0.30

In the table, values computed from simulation are shown in bold type and the upper two rows show previously reported values. From the table it can be seen that the computed values compared favorably to the previously reported values. It was seen that the computed values of the fluorescent yield, probability of K-shell interaction and

probability of K-fluorescence emission did not change with increasing CsI thickness from 250 μm – 600 μm . Escape fraction was computed at an energy just above the K-edge of cesium and iodine (36 keV) and was observed to decrease with increasing thickness. As the scintillator thickness increases, characteristic radiations have more distance to travel and hence the number of characteristic radiations escaping out of the scintillator decreases. Figure 14 shows the probability of K x-ray reabsorption vs. thickness. As the scintillator thickness increases, the probability of reabsorption increases because less K x-rays escape out of the scintillator.

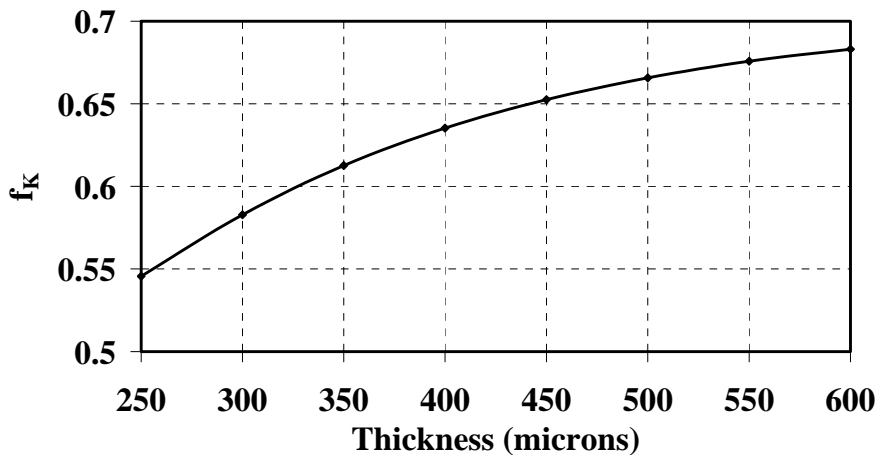


Figure 14: Probability of K x-rays reabsorption vs. thickness.

5.1.2 Distribution of energy along the depth of CsI scintillator

Figure 15 is a plot of the fraction of energy deposited along the depth of a 380 μ CsI scintillator. From the plot it can be seen that the fraction of energy deposited in the first 20 μ of the scintillator decreases as the kVp setting decreases from 30 kVp to 80 kVp. 30

kVp spectra have lower energy x-rays and hence more energy would be absorbed in the first few microns of the scintillator, whereas 80 kVp spectra have higher energy x-rays and hence they would be absorbed deeper inside the scintillator. From the plot, it can also be seen that the fractional energy deposited towards the exit of the scintillator increases from 30 kVp to 80 kVp for the same reason mentioned above. The area under each curve was computed and is reported in Table 2. From the table it can be seen that the area under the curve decreases from 30 kVp to 80 kVp. This is because the 30 kVp spectra have lower energy x-rays and hence a higher probability of being absorbed in the scintillator as compared to x-rays in higher kVp spectra.

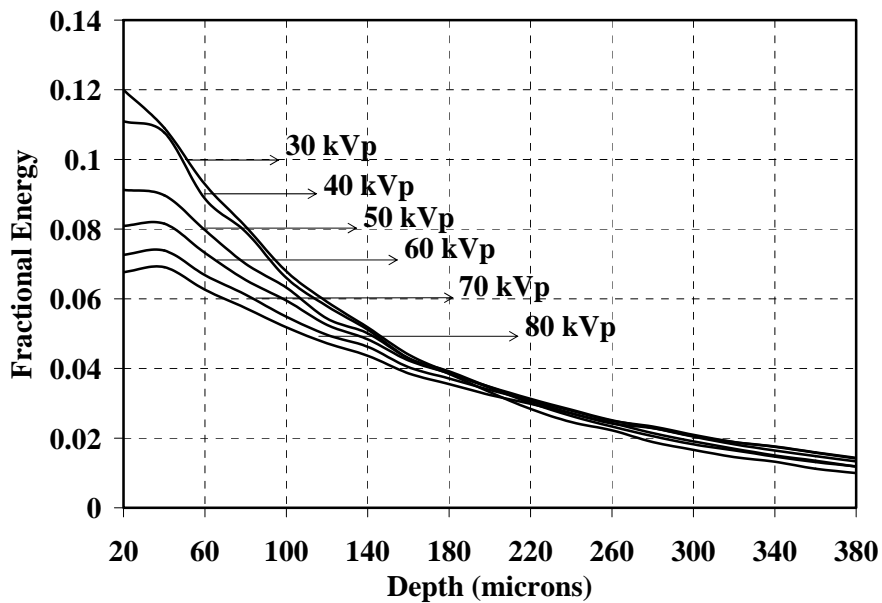


Figure 15: Energy distribution along the depth of CsI scintillator.

Table 2: Area under each of curve of the distribution of the energy along the depth of CsI scintillator.

Spectra (kVp)	30 kVp	40 kVp	50 kVp	60 kVp	70 kVp	80 kVp
Area under each curve	0.8733	0.8357	0.7950	0.7676	0.7306	0.6969

5.1.3 Validation of the simulation

Modulation transfer functions for 100 μ and 300 μ thick CsI scintillator computed from the present study were compared to the results of Vedantham et al [23, 25] to validate the computed simulation. Shown in Figure 16 is the simulated psMTF obtained by modeling the GE prototype digital mammography imager with 100 μ thick CsI, 100 μ pixel size, and using a 28 kVp, Mo/Mo x-ray spectra. Also shown in Figure 16 is the empirically measured psMTF reported by Vedantham et al. [23]. Relatively good agreement between simulated and measured psMTFs is observed.

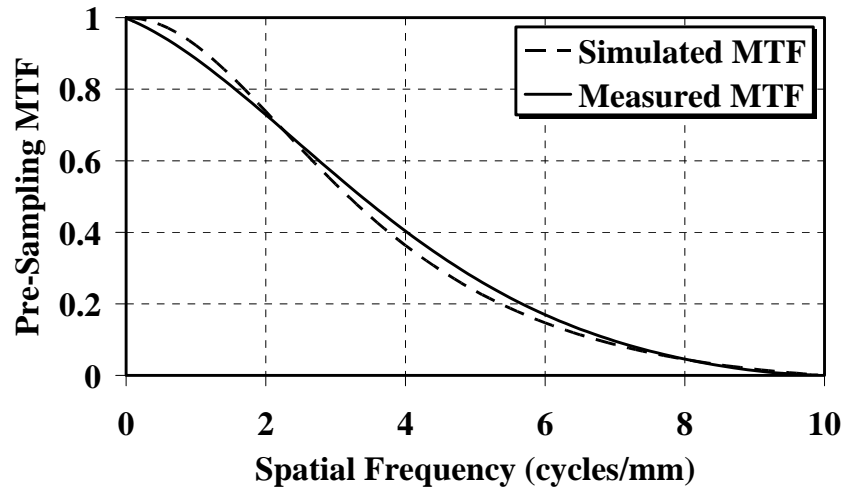


Figure 16: Pre-sampling MTF for 100 μ CsI scintillator.

Figure 17 shows a simulated scintillator MTF (pixel blurring was not modeled here) computed using the 300 μ thick CsI and a 72 kVp W/Al x-ray spectra. This MTF was compared to measurements reported by Vedantham et al [25] for the same CsI thickness and energy spectra, and again relatively good agreement was observed.

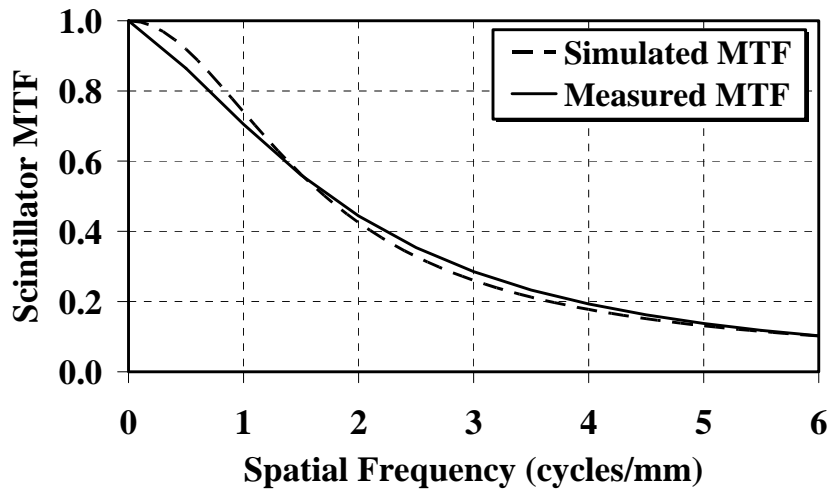


Figure 17: Scintillator MTF for 300 μ CsI scintillator.

The simulated number of digital units per mR per 100 μ m pixel was computed to be 18.9 DU/mR/pixel and the measured sensitivity was reported to be 16.3 DU/mR/pixel [23]. Differences in the simulated and empirically measured sensitivities can be attributed to the many free parameters required in the DETECT-II simulation and the various assumptions made.

5.2 Breast dosimetry

GEANT 3 Monte Carlo software was used to estimate the dose to the breast in the CT geometry. Validation of this software was done by comparing some coefficient values with those in the literature.

5.2.1 Comparison of linear attenuation coefficients

Figure 18 shows a plot of the computed linear attenuation coefficient (μ) values at various energy levels. Also shown in the Figure 18 are the μ values reported in [26, 28]. An excellent agreement is seen between the computed values and those reported in the literature.

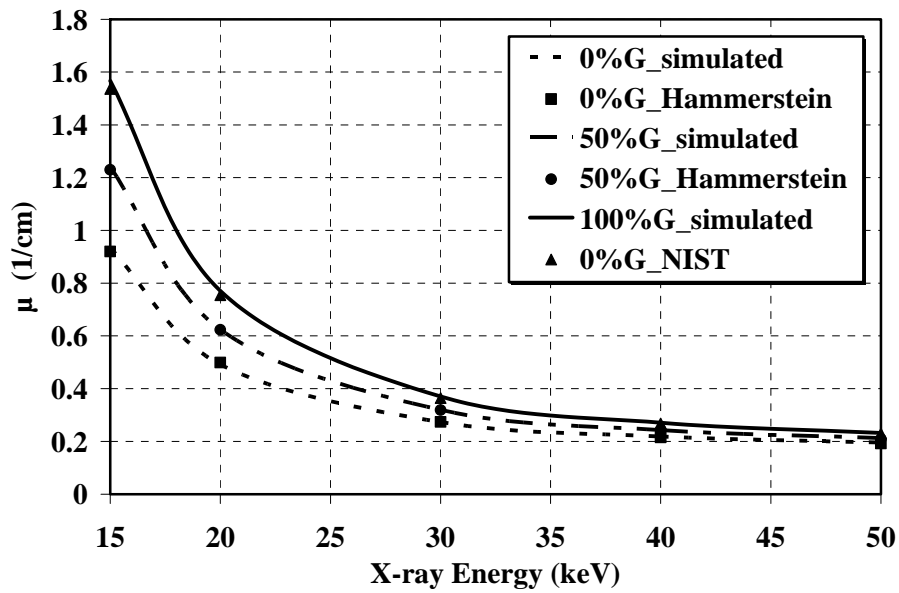


Figure 18: Comparison with linear attenuation coefficients in the literature.

5.2.2 Comparison of DgN coefficients for conventional mammography

Figure 19 shows a comparison of the DgN coefficients computed in the present study using the GEANT 3.21 Monte Carlo code with the data from Boone's study [11] for conventional mammography using a compressed breast model. This comparison was done for breast thicknesses of 2 cm, 6 cm, and 10 cm having 100% glandular breast tissue composition. An excellent correlation was observed as can be seen from the regression

line for breast thicknesses of 10 cm ($r^2 = 0.9997$), 6 cm ($r^2 = 0.9995$) and 2 cm ($r^2 = 0.9984$). A paired T-test was also performed which showed that the difference in the means was not statistically significant ($p = 0.79697$).

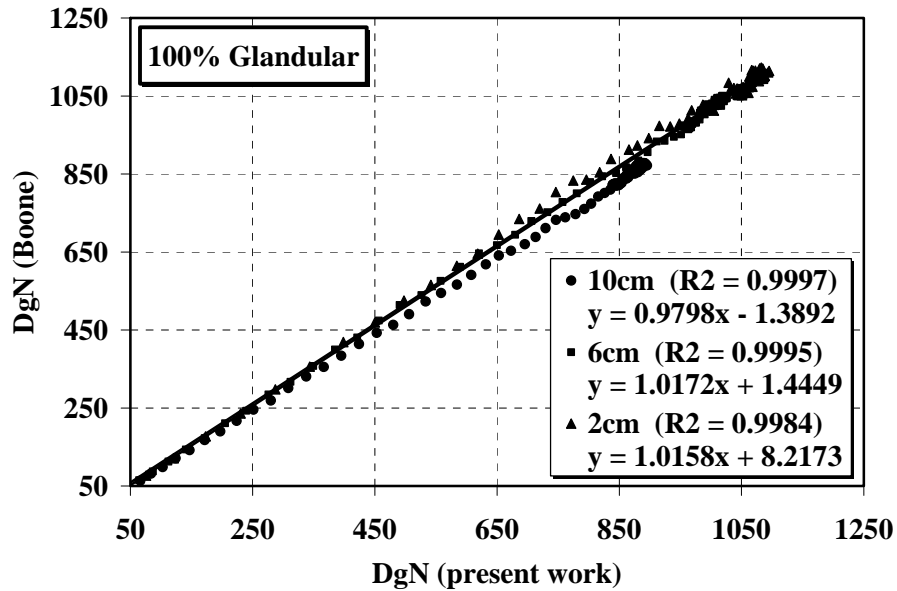
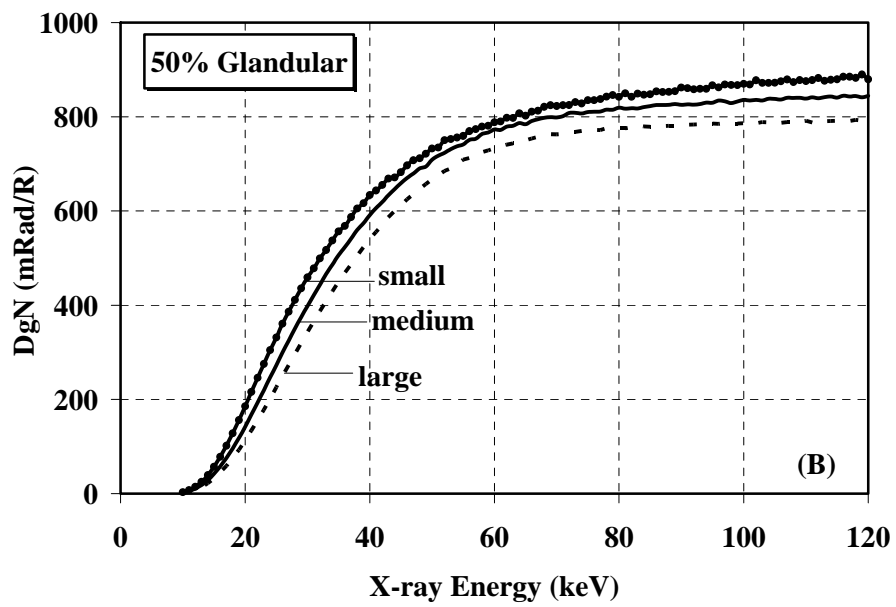
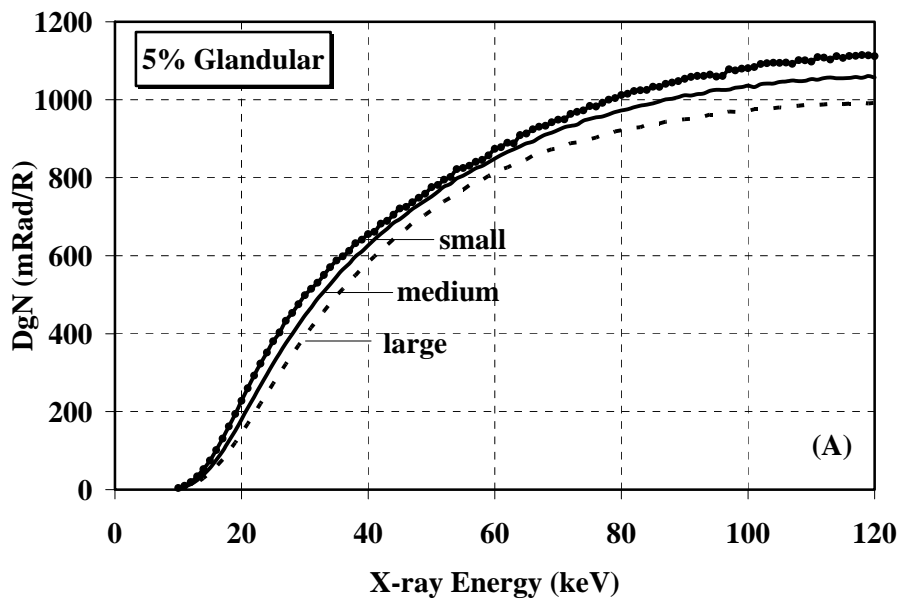


Figure 19: Graph shows a comparison of the DgN values published by Boone [11] along the y-axis with the Monte Carlo derived DgN values in the present study along the x-axis. The data are shown for 100% glandular compressed breast phantom having a breast thickness of 10 cm, 6 cm and 2 cm and an excellent correlation is observed.

5.2.3 DgN coefficients for CT mammography

Figure 20 [A, B, C] shows the Monte Carlo computed DgN values for the uncompressed breast model for monoenergetic x-ray energies corresponding to three breast compositions of 5% glandular, 50% glandular and 100% glandular, respectively, for three different sizes of the breast.



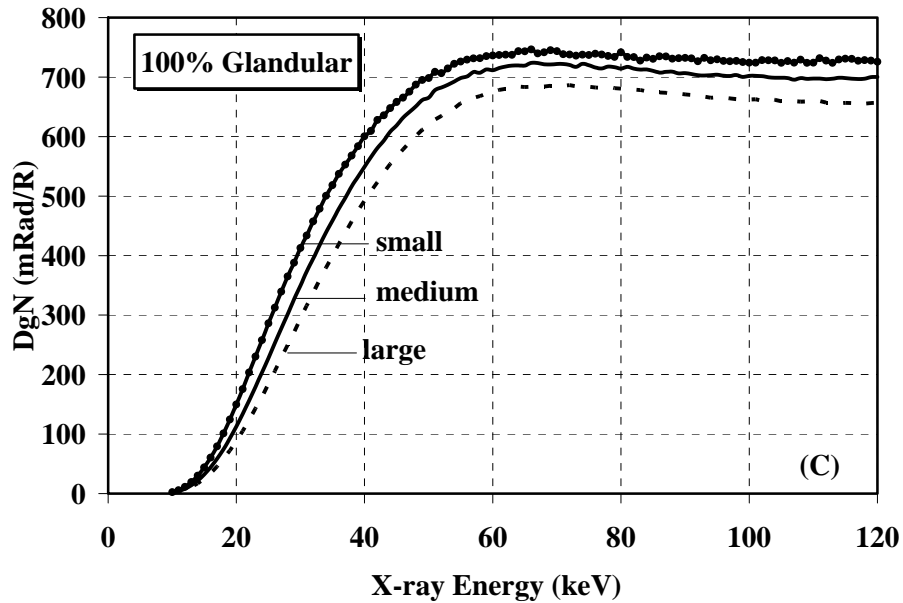


Figure 20: The monoenergetic DgN values computed from Monte Carlo simulations corresponding to three breast compositions of 5% glandular, 50% glandular and 100% glandular respectively are shown in the panels [(A), (B) and (C)] respectively. The data are shown for the three different sizes of the uncompressed breast.

Further, fit equations of the DgN curves were generated using MATLAB to replicate the DgN coefficients for the three sizes of the breast and three compositions of the adipose and glandular tissue for all energies and are included in Appendix [A, B, C]. From this data, the mean glandular dose for any spectrum can also be easily estimated.

The variation in DgN values due to statistical noise was assessed from the coefficient of variation ($100\% * \text{Standard Deviation} / \text{Mean}$) for 5 runs of one millions x-rays per run. The COV was found to be (less than) 0.35 % (averaged over energy and tissue composition) for the smaller-sized breast model. Lower COVs were observed for the other breast model sizes.

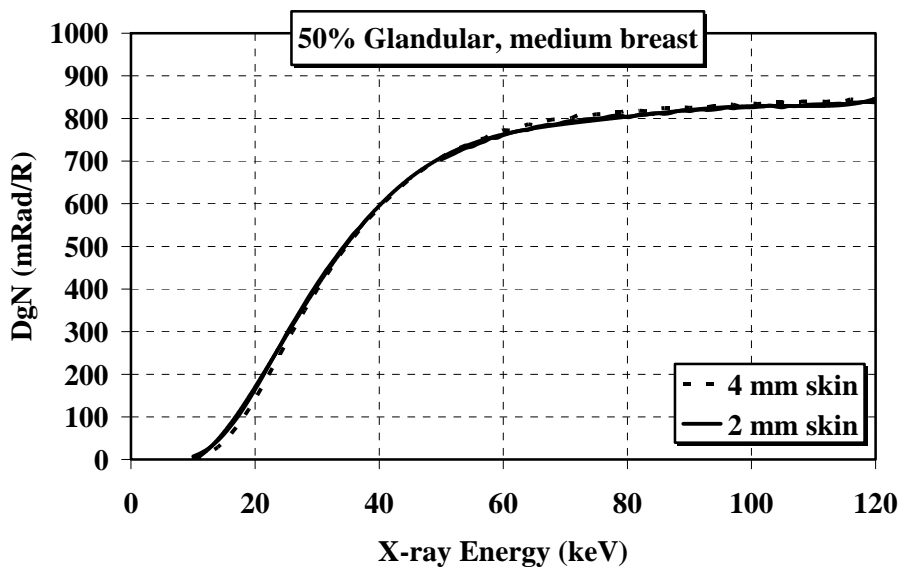


Figure 21: The effect of change in skin thickness (from 4 mm to 2 mm) on DgN values. As seen from the graph, no significant difference was observed over all the energies.

Figure 21 illustrates the effect of change in skin thickness, from 4 mm to 2 mm, on DgN values for a 50% glandular medium-sized breast. Since the spectra to be used for CT mammography would be of higher energy than that used for conventional mammography [24], DgN values for higher energies are reported. Relative to the 4 mm skin thickness, DgN values increased by 3.5% and 0.4% at 30 keV and 40 keV, respectively, and decreased by 0.6% and 1.6% at 50 keV and 60 keV, respectively, for a breast encapsulated by a skin layer of 2 mm thickness.

Figure 22 illustrates the DgN values of a cylindrical breast phantom in comparison with a hemi-ellipsoid breast phantom having a 50% glandular breast tissue composition. The graph shows that the change in DgN values, relative to the cylindrical phantom, that

resulted from the hemi-ellipsoid phantom was 1.2%, 1.07%, 1.6% and 0.95% at 30 keV, 40 keV, 50 keV and 60 keV, respectively. Thus, there is no significant difference between the DgN values, at each energy, of the medium-sized hemi-ellipsoid phantom and the cylindrical breast phantom.

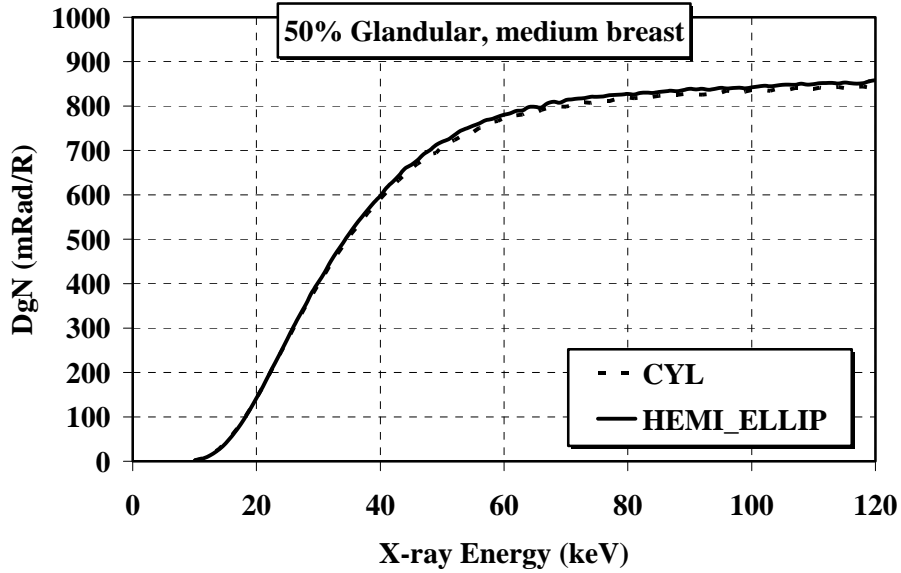
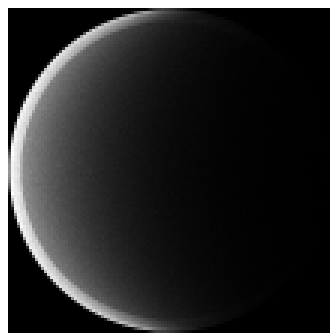
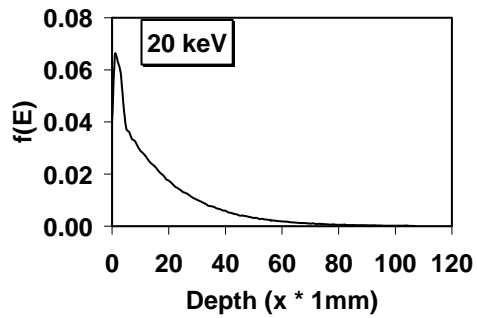


Figure 22: Graph shows a comparison of the DgN values over all the energies of the medium-sized cylindrical breast phantom with the DgN values of the hemi-ellipsoid phantom having a 50% glandular breast tissue composition. The DgN values for the hemi-ellipsoid are higher over all the energies but not a significant difference is observed.



(a)



(e)

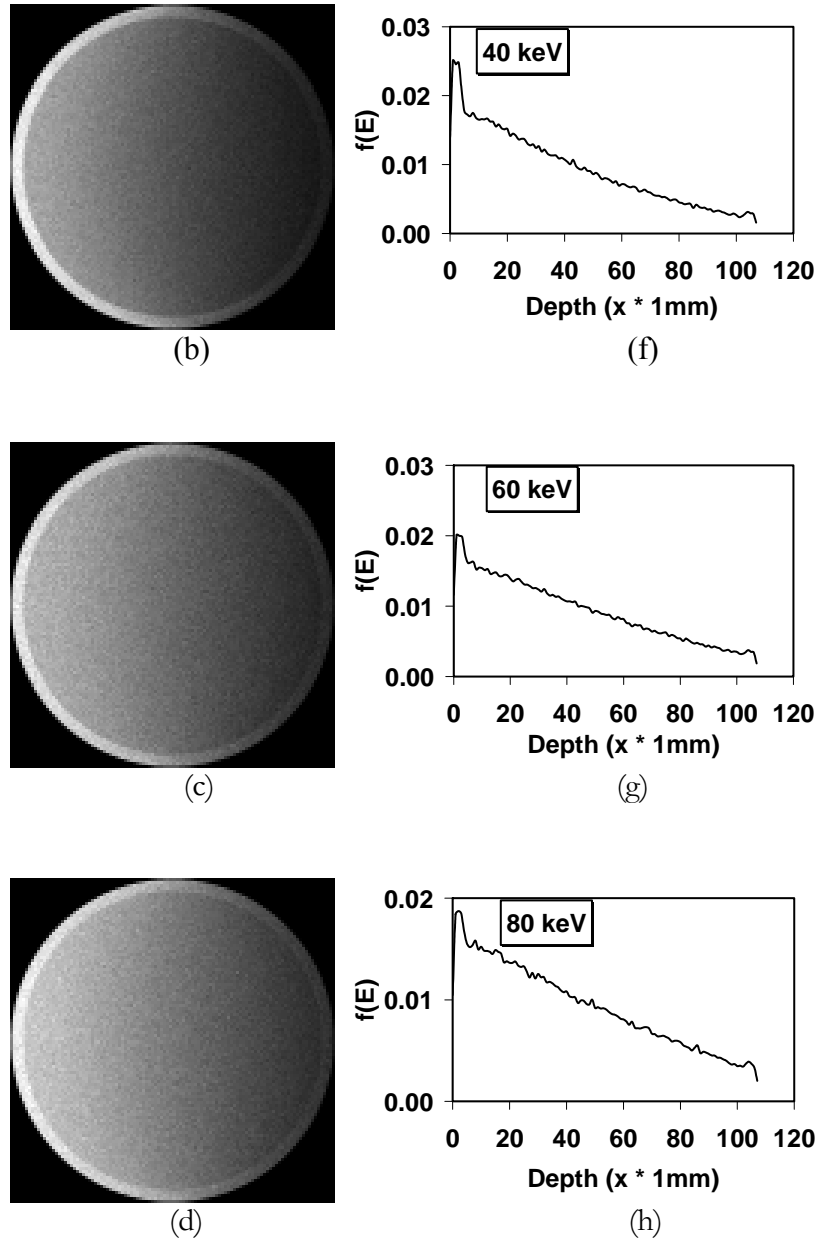


Figure 23: The images of the distribution of the energy deposited in the cylindrical breast phantom having incident energy of 20 keV, 40 keV, 60 keV and 80 keV are shown in panels (a), (b), (c) and (d), respectively. The panels (e), (f), (g) and (h) show the profiles of the fractional energy deposited in the breast versus the depth through the breast.

Figure 23 [a, b, c, d] shows images of the distribution of the energy deposited in the medium-sized cylindrical breast phantom having incident monoenergetic x-ray energy of

20 keV, 30 keV, 40 keV and 50 keV, respectively. From these images, it can be seen that the amount of energy deposited along the depth through the breast increases with the increase in the incident energy as higher energy x-rays tend to travel farther through the tissue. Figure 23 [e, f, g, h] show the profiles of the fraction of the total energy deposited versus the depth through the breast with incident monoenergetic x-ray energy of 20 keV, 30 keV, 40 keV and 50 keV, respectively. As expected, these profiles show that the fraction of energy deposited in the skin decreases with increase in the incident energy.

Chapter 6

CONCLUSION

A computer simulation was developed to model the CsI-based a:Si flat panel detector. The simulation provided a means for estimating various parameters associated with the serial and parallel cascade models that were needed in computing figures-of-merit for volumetric breast imaging systems. These computed parameters compared favorably with those reported in the literature.

Simulations of a commercial prototype CsI-based digital mammography system showed good agreement between the psMTFs, and system sensitivity obtained with simulated and experimental measurements. A good agreement was also observed between the scintillator MTFs of 300 μm thick CsI scintillator. System sensitivity is dependent on a number of free parameters. Therefore, further studies should be done to investigate the choice of DETECT-II parameters, fill-factor, scintillation yield, and their effect on system sensitivity and corresponding effect on the modulation transfer function.

A computer simulation was also developed to estimate the radiation dose to the breast in the CT geometry. The simulation was validated as the results of the simulated linear attenuation coefficients and the DgN coefficients compared very well to those reported in the literature. The simulation was further modified to estimate the normalized glandular dose to the uncompressed breast in CT mammography. Furthermore, fit equations of the normalized glandular dose curves were generated using MATLAB to replicate the DgN

coefficients for the three sizes of the breast and three compositions of the adipose and glandular tissue for all energies. From this data, the mean glandular dose for any spectra can also be easily estimated.

The simulation can also be used to form projection images. Hence, a simple model of the breast can be simulated using a realistic x-ray spectrum, and the projection images of the breast formed at different source angles can be reconstructed using filtered back projection algorithm for cone-beam geometry.

Thus it can be concluded that the computer simulation can be used to conduct further studies to understand various interactions mechanisms in the CsI scintillator and to model the cascaded models. It can also be concluded that the computer simulation not only provides a means for comparing the potential performance of the existing systems but also provides a means for optimizing imaging system performance.

REFERENCES

1. United States Institute of Medicine, National Research Council, *Mammography and Beyond: Developing Technologies for the Early Detection of Breast Cancer*, p. 2, 2001.
2. M. J. Yaffe, Chapter 5, *Handbook of medical imaging, vol. 1, Physics and Psychophysics*.
3. <http://www.spectrum.ieee.org/WEBONLY/pressrelease/0501/cancer0501.pdf>
4. CERN 1993, Geant 3.21, *Detector description and simulation tool, CERN program library long write-up*, Geneva, Switzerland.
5. A. Badano, R. Leimbach, “Depth-dependent phosphor blur in indirect x-ray imaging sensors,” *4682*, 94-106, SPIE, San Diego, CA, 2002.
6. Dose efficiency and low-contrast detectability of anamorphous silicon x-ray detector for digital radiography, Richard Aufrichtig and Ping Xue, *Phys. Med. Biol.* **45**, 2653–2669, 2000.
7. M. P. Eckstein, C. K. Abbey, F. O. Bochud, Chapter 10, *Handbook of medical imaging, vol. 1, Physics and Psychophysics*.
8. J. Yao and I. A. Cunningham, “Parallel cascades: New ways to describe noise transfer in medical imaging systems,” *Med. Phys.* **28** (10), October 2001.
9. J. H. Siewerdsen, L. E. Antonuk, Y. el-Mohri, et al, “Empirical and theoretical investigation of the noise performance of indirect detection, active matrix flat-panel imagers (AMFPIs) for diagnostic radiology,” *Med Phys.* **24** (1), January 1997.

10. H. H. Barrett, R. F. Wagner, K. J. Myers, "Correlated point processes in radiological imaging," *3032*, 110-124, SPIE, Newport Beach, CA, 1997.
11. J. M. Boone, "Glandular breast dose for monoenergetic and high-energy x-ray beams: Monte Carlo assessment," *Radiology* **213**, 23-37, 1999.
12. R. Ning, "Apparatus and Method for Cone Beam Volume Computed Tomography Breast Imaging," *United States Patent*, Patent No. US 6,480,565 B1, 2002.
13. J. M. Boone, "Normalized glandular dose (DgN) coefficients for arbitrary x-ray spectra in mammography: Computer-fit values of Monte Carlo derived data," *Med Phys.* **24** (5), May 2002.
14. J. M. Boone, N. Shah, T. R. Nelson, "A comprehensive analysis of DgN_{CT} coefficients for pendant-geometry cone-beam breast computed tomography," *Med Phys.* **31** (2), February 2004.
15. J. M. Boone, A. Seibert, "An accurate method for computer generating tungsten anode X-ray spectra from 30 to 140 kV", *Med. Phys.* **24** (11), 1661-1670, 1997.
16. I. A. Cunningham, J. Yao, V. Subotic, "Cascaded models and the DQE of flat-panel imagers: noise aliasing, secondary quantum noise and reabsorption," *4682*, 61-72, SPIE, San Diego, CA, 2002.
17. W. Hillen, W. Eckenbach, P. Quadflieg, T. Zaengel, "Signal-to-noise performance in cesium iodide x-ray fluorescent screens," *1443*, 120-131, SPIE, San Jose, CA, 1991.
18. I. Holl, E. Lorenz, G. Mageras, "A measurement of light yield of common inorganic scintillators," *IEEE Transactions on Nuclear Science* **35** (1), 105-109, 1988.

19. T. Jing, C.A. Goodman, G. Cho, J. Drewery, W.S. Hong, H. Lee, S. N. Kaplan, A. Mireshghi, V. Perez-Mendez, D. Wildermuth, "Amorphous Silicon Pixel Layers with Cesium Iodide Converters for Medical Radiography," IEEE Nuclear Science Symposium, San Francisco, CA, 1993.
20. V. Perez-Mendez, G. Cho, J. Drewery, T. Jing, S. N. Kaplan, A. Mireshghi, D. Wildermuth, "Amorphous Silicon radiation detectors and associated thin film transistor electronics readout," Lawrence Berkeley Lab Publication No. 32460.
21. P. B. Catrysse and B. A. Wandell, "Optical efficiency of image sensor pixels," *Journal of the Optical Society of America A*, **19** (8), 1610-1620, 2002.
22. W. Viehmann, J. F. Arens, and M. Simon. Optical transmission measurements on monocrystalline and polycrystalline cesium iodide. *Nuclear Instruments and Methods*, **116**, 283-295, 1974.
23. Vendantham et al, "Full breast digital mammography with an amorphous silicon-based flat panel detector: Physical characteristics of a clinical prototype," *Med. Phys.* **27** (3), March 2000.
24. S. J. Glick, S. Vedantham, A. Karellas, "Investigation of optimal kVp settings for CT mammography using a flat-panel imager," *4682*, 392-402, SPIE, San Diego, CA, 2002.
25. S. Vendantham, *Design and characterization of a high-resolution cardiovascular imager*, PhD dissertation, Worcester Polytechnic Institute, Worcester, MA, 2002.
26. R. G. Hammerstein, D. W. Miller, D. R. White, et al, "Absorbed Radiation Dose in Mammography", *Radiology* **130**, 485-491, 1979.

27. L. E. Wilkinson and J. C. P. Heggie, "Glandular Breast Dose: Potential Errors," *Radiology* E-letter, **213**/1/23, 2000.
28. <http://physics.nist.gov/PhysRefData/XrayMassCoef/ComTab/cesium.html>
29. C. L. Kalbhen, J. J. McGill, P. M. Fendley, et al, "Mammographic Determination of Breast Volume: Comparing Different Methods," *American Journal of Roentgenology*, **173**, 1643-1649, 1999.
30. D. B. Kopans, *Breast Imaging*, 2nd edn, Philadelphia: Lippincott-Raven, p. 3-4, 1998.
31. Shu-Jen Lee, Corinne Groiselle, *Operating procedure for DETECT-II simulation*. (For internal use, not published)

Appendix A

Fit-equations for small-sized breast model

$$DgN(E) = a \times E^9 + b \times E^8 + c \times E^7 + d \times E^6 + e \times E^5 + f \times E^4 + g \times E^3 + h \times E^2 + i \times E + j$$

	100%	50%	5%
a	-3.9559×10^{-14}	-6.064×10^{-14}	-1.8925×10^{-13}
b	2.4962×10^{-11}	4.2594×10^{-11}	1.2284×10^{-10}
c	-6.9483×10^{-9}	-1.2933×10^{-8}	-3.4369×10^{-8}
d	1.1292×10^{-6}	2.2209×10^{-6}	5.4134×10^{-6}
e	-0.00011904	-0.00023674	-0.00052548
f	0.0084546	0.016137	0.032296
g	-0.39719	-0.69379	-1.2389
h	11.175	17.478	27.791
i	-138.95	-201.83	-296.08
j	603.29	832.77	1153.4

Appendix B

Fit-equation for medium-sized breast model

$$DgN(E) = a \times E^9 + b \times E^8 + c \times E^7 + d \times E^6 + e \times E^5 + f \times E^4 + g \times E^3 + h \times E^2 + i \times E + j$$

	100%	50%	5%
a	5.8598×10^{-14}	2.2331×10^{-14}	-6.5051×10^{-14}
b	-3.5892×10^{-11}	-1.0828×10^{-11}	4.5906×10^{-11}
c	9.3098×10^{-9}	1.8417×10^{-9}	-1.3967×10^{-8}
d	-1.3162×10^{-6}	-6.8166×10^{-8}	2.3938×10^{-6}
e	0.00010758	-1.9757×10^{-5}	-0.00025326
f	-0.0048185	0.0032674	0.017022
g	0.0849	-0.22676	-0.71779
h	1.0532	7.8442	17.759
i	-33.878	-105.44	-203.17
j	191.45	472.64	834.65

Appendix C

Fit-equation for large-sized breast model

$$DgN(E) = a \times E^9 + b \times E^8 + c \times E^7 + d \times E^6 + e \times E^5 + f \times E^4 + g \times E^3 + h \times E^2 + i \times E + j$$

	100%	50%	5%
a	5.9413×10^{-14}	3.4939×10^{-14}	-1.5848×10^{-14}
b	-3.8457×10^{-11}	-2.1142×10^{-11}	1.4005×10^{-11}
c	1.0627×10^{-8}	5.3551×10^{-9}	-5.0439×10^{-9}
d	-1.6237×10^{-6}	-7.233×10^{-7}	9.8985×10^{-7}
e	0.00014766	5.3612×10^{-5}	-0.00011766
f	-0.0079295	-0.0017954	0.0088107
g	0.22814	-0.015888	-0.41343
h	-2.5948	2.9235	11.361
i	8.9661	-51.362	-138.8
j	9.7856	255.03	595.4

Appendix D

Operating procedure for GEANT 3 simulation [4]

GEANT 3: In GEANT 3, there are many input files, for example, USRDET.F is for geometry definition, USRMATE.F is for material definition. RUN_SIMULATION.CSH is a configuration file to define a number of other parameters.

RUN_SIMULATION.CSH is a shell script and some of the parameters defined in this file are as follows:

- seed to run the simulation;
- file number;
- number of annihilations;
- distance between the source and the detector;
- activity of the photons in keV;
- position of the x-ray tube;
- size of the detector (crystal) and
- various flags for different interaction mechanisms.

Configuration file (RUN_SIMULATION.CSH) (shell script):

```
#!/bin/csh  
  
#####  
# Copy the files for limited emission cone #  
#####  
cp direction.f.limited.hd1 direction.f
```

```

#####
# Compilation of GEANT 3.21 #
#####

#./simcomp_w

#####
# Variables setup - to be modified by user #
#####

set MY_DIR = "/chucky/geant3.21/my_geant/"

# SEED to run the simulation
set i = 50

# File number
set prefix = $argv[1]

# Scatter (0=no, 1=short cylinder, 2=long cylinder, 3=BREAST, 5=WB)
set scatter=3

# Number of annihilations
set trigger=$argv[2]

# Distance between the detector and the X-ray tube
set ra=100.

# Activity in kev
set a = $argv[3]
echo $a

# Position of the X-Ray tube
set x=0.
set y=0.
set z=9.5

# Crystal size
set s1=32.
set s2=32.
set s3=0.01

# Variable for the listmode(3=lst,4=erg,5=elec,6=frac,7=psf)
set mode=3

```

```

#####
# Create the card file #
#####
set ffr_file=$MY_DIR${prefix}_${a}.ffr
echo $ffr_file

#####
# Create the pcd4_###.ffr card #
#####
echo 'C ----- C' >> $ffr_file
echo 'C C' >> $ffr_file
echo 'C FRREAD PARAMETER CARDS FOR GEANT C' >> $ffr_file
echo 'C C' >> $ffr_file
echo 'C Executable version : PCD4.8 - redefined head geometries C' >> $ffr_file
echo 'C Run number : ### (example for UMass) C' >> $ffr_file
echo 'C Owner : Jeff Kolthammer C' >> $ffr_file
echo 'C Date : 23 Jan 01 C' >> $ffr_file
echo 'C C' >> $ffr_file
echo 'C All length dimensions are (cm) unless otherwise quoted C' >> $ffr_file
echo 'C C' >> $ffr_file
echo 'C ----- C' >> $ffr_file
echo 'C' >> $ffr_file

echo 'C -----GENERAL RUN PARAMETERS-----' >> $ffr_file
echo 'C' >> $ffr_file
echo 'C TRIG = Number of tracked events to use' >> $ffr_file
echo 'C RNDM = sets random number seeds.' >> $ffr_file
echo 'C' >> $ffr_file
echo 'LIST' >> $ffr_file
echo 'TRIG $trigger >> $ffr_file
echo 'TRIG $trigger
echo 'SWIT 2' >> $ffr_file
echo 'RNDM $i.' >> $ffr_file
echo 'C' >> $ffr_file
echo 'C ROTATION INFO' >> $ffr_file
echo 'C -----' >> $ffr_file
echo 'C #_proj(0=continuous) cor(3) rot_axis(1=x,2=y,3=x) angle(in degrees)' >>$ffr_file
echo 'UROTATE 1. 0. 0. 0. 2. 0.' >> $ffr_file
echo 'C' >> $ffr_file
echo 'C SCATTER INFO' >> $ffr_file
echo 'C -----' >> $ffr_file
echo 'USCAT $scatter.' >> $ffr_file
echo 'C' >> $ffr_file

```

```

echo 'C EMISSION INFO' >> $ffr_file
echo 'C -----' >> $ffr_file
echo 'UPHAN 1 '$a' '$x' '$y' '$z' 90. 2. 0. 0. 0. 0. 0. 0.' >> $ffr_file
echo 'UPHAN 1 '$a' '$x' '$y' '$z' 90. 2. 0. 0. 0. 0. 0. 0.'
echo 'C' >> $ffr_file
echo 'C ----WORLD-SPACE GEOMETRY AND RUN PARAMETERS-----'>>$ffr_file
echo 'C' >> $ffr_file
echo 'C DETECTOR' >> $ffr_file
echo 'C -----' >> $ffr_file
echo 'C number_heads default_radius listmode emission_rate resolution' >> $ffr_file
echo 'UDET 2.'$ra"$mode 37000. .41' >> $ffr_file
echo 'C *note: radius measures cor to face of crystal' >> $ffr_file
echo 'C' >> $ffr_file
echo 'C HEADWISE - individual radius, theta, tangential_shift' >> $ffr_file
echo 'C -----' >> $ffr_file
echo 'URHEAD '$ra' '$ra' 0. 0. 0. 0. 0. 0.' >> $ffr_file
echo 'UTHEAD 90. 270. 0. 0. 0. 0. 0. 0.' >> $ffr_file
echo 'USHEAD 0. 0. 0. 0. 0. 0. 0. 0.' >> $ffr_file
echo 'C' >> $ffr_file
echo 'C -----HEAD-SPACE GEOMETRY-----' >> $ffr_file
echo 'C' >> $ffr_file
echo 'C DIMENSIONS OF XTAL AND GLASS' >> $ffr_file
echo 'C -----' >> $ffr_file
echo 'C crystal_size(3) glass_size(3) 1.905 = 3/4" thick crystal' >> $ffr_file
echo 'C UNAI '$s1' '$s2' '$s3' 61.83 49.53 1.5875' >> $ffr_file
echo 'UNAI '$s1' '$s2' '$s3' 0. 0. 0.' >> $ffr_file
echo 'C *note: most components have (x,y) same as glass ' >> $ffr_file
echo 'C' >> $ffr_file
echo 'C THICKNESS OF OTHER COMPONENTS' >> $ffr_file
echo 'C -----' >> $ffr_file
echo 'C pan gap iface pmt gasket plate gap inner outer frontframe' >> $ffr_file
echo 'C UPCD .127 .175 .076 10.599 .546 1.029 2.017 .795 .795 1.905' >> $ffr_file
echo 'UPCD 0. 0. 0. 0. 0. 0. 0. 0. 0.' >> $ffr_file
echo 'C *note: pan and plate are Al' >> $ffr_file
echo 'C inner and outer are Pb' >> $ffr_file
echo 'C gaps, iface, pmt, gasket are vacuum' >> $ffr_file
echo 'C' >> $ffr_file
echo 'C -----HEAD ATTACHMENT OPTIONS-----' >> $ffr_file
echo 'C' >> $ffr_file
echo 'C GENERAL OPTIONS' >> $ffr_file
echo 'C -----' >> $ffr_file
echo 'C z_aluminum z_plastic z_gap frame septa phole (1=on 0=off)' >> $ffr_file
echo 'C UHAGO .0508 .0381 .2972 0. 0. 0.' >> $ffr_file
echo 'UHAGO 0. 0. 0. 0. 0. 0.' >> $ffr_file

```



```

echo 'C' >> $ffr_file
echo 'C SCATTER SHIELD' >> $ffr_file
echo 'C -----' >> $ffr_file
echo 'C mat z mat z mat z mat z (order hit by photon, up to 5 layers)' >> $ffr_file
echo 'UFRAM 3. .04 12. .08 16. .01 1. .127 0. 0.' >> $ffr_file
echo 'C Pb Sn Cu Al' >> $ffr_file
echo 'C' >> $ffr_file
echo 'C AXIAL SEPTA' >> $ffr_file
echo 'C -----' >> $ffr_file
echo 'C material thickness depth gap_size' >> $ffr_file
echo 'USLAT 3. 0.23 3.5 0.77' >> $ffr_file
echo 'C' >> $ffr_file
echo 'C PARALLEL-HOLE COLLIMATOR' >> $ffr_file
echo 'C -----' >> $ffr_file
echo 'C material hole_radius hole_depth hole_pitch' >> $ffr_file
echo 'UCOLL 3. 0.17 7.2 .54' >> $ffr_file
echo 'C' >> $ffr_file

echo 'C -----OTHER >> ffr_file RUN CONTROL CARDS-----' >> $ffr_file
echo 'C' >> $ffr_file
echo 'DEBU 1 100' >> $ffr_file
echo 'SWIT 2' >> $ffr_file
echo 'CUTS 0.000001 0.000001' >> $ffr_file
echo 'PHOT 1' >> $ffr_file
echo 'PAIR 1' >> $ffr_file
echo 'COMP 1' >> $ffr_file
echo 'RAYL 1' >> $ffr_file
echo 'AUTO 0' >> $ffr_file
echo 'ABAN 1' >> $ffr_file
echo 'ERAN .00001 .01000 199' >> $ffr_file
echo 'LOSS 1' >> $ffr_file
echo 'C DRAY 1' >> $ffr_file
echo 'STOP' >> $ffr_file
echo 'END' >> $ffr_file

#####
# Run the simulation #
#####
./simrun_w $a

```

List of Run Control Cards (Flags):

- **DEBU 1 100** for debugging
 - DEBU first event to debug last event to debug.

- **SWIT 2** user flags for debug
 - 2 current information on the track is printed to the LOG file.

- **CUTS 0.000001 0.000001** minimum energy cut
CUTS [cutgam cutele]
 - cutgam minimum energy cut for electrons;
 - cutele minimum energy cut for gammas.

- **PHOT 1** photo electric effect
 - 0 no photo electric effect;
 - 1 photoelectric effect, electron processed;
 - 2 photoelectric effect, no electron stored.

- **PAIR 1** pair production
 - 0 no pair production;
 - 1 pair production, secondaries processed;
 - 2 pair production, no secondaries stored.

- **COMP 1** compton scatter
 - 0 no compton;
 - 1 compton, electron processed;
 - 2 compton, no electron stored.

- **RAYL 1** Rayleigh scatter
 - 0 no Rayleigh scattering;
 - 1 Rayleigh scattering.

- **AUTO 0** automatic computation of the tracking

 medium parameters
 - 0 no automatic calculation;
 - 1 automatic calculation.

- **ABAN 1** stop following the photons if it exits the

 volume.
 - > 0

- **ERAN .00001 .01000 199** cross-section tables structure

 ERAN [ekmin, ekmax, nekbin]
 - ekmin minimum energy of the tables;
 - ekmax maximum energy of the tables;
 - nekbin number of bins in the tables.

- **LOSS 1**
 - 0 energy loss;
 - 1 no energy loss;
 - 2 restricted energy loss fluctuations;
 - 3 complete energy loss fluctuations;
 - 4 same as 1;
 - 5 no energy loss fluctuations.

- **C DRAY 1**
 - 0 delta ray
 - 1 no delta rays;
 - 2 delta rays, secondaries processed;
 - 3 delta rays, no secondaries stored.

Geometry of the volumes used (USRDET.F):

```
C=====
C *** Define the MOTHER Volume as a 500x500x500 cm cube ***
C=====

SIZE(1) = 250.0 ! 1/2 length along the x-axis
SIZE(2) = 250.0 ! 1/2 length along the y-axis
SIZE(3) = 250.0 ! 1/2 length along the z-axis

call GSVOLU('WRLD','BOX ',6, SIZE, 3, IRC) ! Material 6 = vacuum

if (IRC .le. 0) then
  write(6,*) 'USRDET error: GSVOLU WRLD rc=',IRC
end if

C=====
C *** BREAST DEFINITION ***
C=====

if (usrscat(1) .eq. 3) then

C=====
C   WATER CYLINDER
C=====

SIZE(1) = 0. ! Rmin
SIZE(2) = 15. ! Rmax
SIZE(3) = 12.5 ! 1/2 length in z

call GSVOLU('CYLW','TUBE',7,SIZE,3,IRC) ! Material 7 = Water

if (IRC .le. 0) then
  write(6,*) 'USRDET error: GSVOLU CYLW rc=',IRC
end if

x = 60.
y = 0.
z = 24.5

call GSROTM(9, 90.,90.,0.,0.,90.,0.)
call GSPOS('CYLW', 1, 'WRLD', x, y, z, 9, 'ONLY')
```

```
C=====
C  SKIN CYLINDER
C=====
```

```
SIZE(1) = 4.6    ! Rmin
SIZE(2) = 5.0    ! Rmax
SIZE(3) = 3.55   ! 1/2 length in z
```

```
call GSVOLU('CYL1','TUBE',34,SIZE,3,IRC) ! Material 34 = Skin
```

```
if (IRC .le. 0) then
  write(6,*) 'USRDET error: GSVOLU CYL1 rc=',IRC
end if
```

```
x = 60.
y = 0.
z = 5.95
```

```
call GSPOS('CYL1', 1, 'WRLD', x, y, z, 0, 'ONLY')
```

```
C=====
C  BREAST TISSUE CYLINDER
C=====
```

```
SIZE(1) = 0.    ! Rmin
SIZE(2) = 4.6   ! Rmax
SIZE(3) = 3.55  ! 1/2 length in z
```

```
call GSVOLU('CYL2','TUBE',32,SIZE,3,IRC) ! Material 32 = 50% G
```

```
if (IRC .le. 0) then
  write(6,*) 'USRDET error: GSVOLU CYL2 rc=',IRC
end if
```

```
x = 60.
y = 0.
z = 5.95
```

```
call GSPOS('CYL2', 1, 'WRLD', x, y, z, 0, 'ONLY')
```

```
C=====
C  SKIN CYLINDER
C=====
```

```
SIZE(1) = 0.    ! Rmin
SIZE(2) = 5.0   ! Rmax
SIZE(3) = 0.2   ! 1/2 length in z
```

```
call GSVOLU('CYL3','TUBE',34,SIZE,3,IRC) ! Material 34 = Skin
```

```
if (IRC .le. 0) then
  write(6,*) 'USRDET error: GSVOLU CYL3 rc=',IRC
end if
```

```
x = 60.
y = 0.
z = 2.2
```

```
call GSPOS('CYL3', 1, 'WRLD', x, y, z, 0, 'ONLY')
```

```
end if
```

```
C=====
C ***CREATE CRYSTAL***
C=====
```

```
SIZE(1) = usrnai(1)/2.  ! crystal is smaller (x,y) than glass
SIZE(2) = usrnai(2)/2.
SIZE(3) = usrnai(3)/2.
```

```
call GSVOLU('XTAL','BOX ', 21, SIZE, 3, IRC) ! material 21 = neutronium
```

```
if (IRC .le. 0) then
  write(6,*) 'USRDET error: GSVOLU XTAL rc=',IRC
end if
```

```
z = naisize/2. - usrpcd(10) - usrpcd(1) - usrpcd(2) - usrnai(3)/2.
```

```
C  fixed distance from front
```

```
call GSPOS('XTAL',1,'NAI ', 0., 0., z, 0, 'ONLY')
```

Description of the various functions called to define the geometry:

Creation of a volume using the function GSVOLU: Defines a volume with a given name, shape, tracking medium number and shape parameters.

CALL GSVOLU (CHNAME, CHSHAP, NMED, PAR, NPAR, IVOLU)

CHNAME (CHARACTER*4) volume name – it must be unique;

CHSHAP (CHARACTER*4) name of one of the GEANT shapes;

NMED (INTEGER) tracking medium number for the volume – from usrmate.F file;

PAR (REAL) array containing the shape parameters;

NPAR (INTEGER) number of parameters defined;

IVOLU (INTEGER) internal volume number – if ≤ 0 an error condition has happened.

Positioning a volume inside its mother using the function GSPOS: Places a copy of a volume previously defined by a call to GSVOLU inside its mother volume CHMOTH.

CALL GSPOS (CHNAME, NR, CHMOTH, X, Y, Z, IROT, CHONLY)

CHNAME (CHARACTER*4) name of the volume being positioned;

NR (INTEGER) copy number of the volume CHNAME being positioned;

CHMOTH (CHARACTER*4) name of the volume in which copy NR of CHNAME is positioned;

X (REAL) x position of the volume in the mother reference system;

Y (REAL) y position of the volume in the mother reference system;

Z (REAL) z position of the volume in the mother reference system;

IROT (INTEGER) rotation matrix number describing the orientation of the volume relative to the coordinate system of the mother;

CHONLY (CHARACTER*4) flag to indicate whether a point found to be in this volume may also be in other volumes which are not direct descendants of it – possible values are ONLY and MANY.

Rotation Matrices which defines the relative position of a volume inside its mother: A

rotation matrix is described to GEANT by giving the polar and azimuthal angles of the axes of the DRS (x' , y' , z') in the MRS via the routine GSROTM.

CALL GSROTM (IROT, THETA1, PHI1, THETA2, PHI2, THETA3, PHI3)

IROT (INTEGER) number of rotation matrix;

THETA1 (REAL) polar angle for axis x' ;

PHI1 (REAL) azimuthal angle for axis x' ;

THETA2 (REAL) polar angle for axis y' ;

PHI2 (REAL) azimuthal angle for axis y' ;

THETA3 (REAL) polar angle for axis z' ;

PHI3 (REAL) azimuthal angle for axis z' .

Material definition (USRMATE.F):

```
C=====
C ***Tissue, 5% G 95% A, by weight (From Boone) ***
C=====

amat(1) = 1.00794      ! H
amat(2) = 12.011      ! C
amat(3) = 14.00674    ! N
amat(4) = 15.9994     ! O
amat(5) = 39.098      ! K
amat(6) = 30.99773762 ! P
amat(7) = 32.068      ! S
amat(8) = 40.078      ! Ca

zmat(1) = 1.
zmat(2) = 6.
zmat(3) = 7.
zmat(4) = 8.
zmat(5) = 19.
zmat(6) = 15.
zmat(7) = 16.
zmat(8) = 20.

weight(1) = .1115
weight(2) = .59725
weight(3) = .01775
weight(4) = .2723
weight(5) = .0003
weight(6) = .0003
weight(7) = .0003
weight(8) = .0003

call GSMIXT(56, '5%GL$', amat, zmat, 0.9331, 8, weight)
```

C

C ***Tissue, 50% G 50% A, by weight (From Boone) ***

C

amat(1) = 1.00794 ! H
amat(2) = 12.011 ! C
amat(3) = 14.00674 ! N
amat(4) = 15.9994 ! O
amat(5) = 39.098 ! K
amat(6) = 30.99773762 ! P
amat(7) = 32.068 ! S
amat(8) = 40.078 ! Ca

zmat(1) = 1.
zmat(2) = 6.
zmat(3) = 7.
zmat(4) = 8.
zmat(5) = 19.
zmat(6) = 15.
zmat(7) = 16.
zmat(8) = 20.

weight(1) = .10700
weight(2) = .40100
weight(3) = .02500
weight(4) = .46400
weight(5) = .00075
weight(6) = .00075
weight(7) = .00075
weight(8) = .00075

call GSMIXT(49, '50% A 50% G\$', amat, zmat, 0.9819, 8, weight)

```
C=====
C ***Tissue, 100% G 0% A, by weight (From Boone) ***
C=====
```

```
amat(1) = 1.00794      ! H
amat(2) = 12.011      ! C
amat(3) = 14.00674    ! N
amat(4) = 15.9994     ! O
amat(5) = 39.098      ! K
amat(6) = 30.99773762 ! P
amat(7) = 32.068      ! S
amat(8) = 40.078      ! Ca
```

```
zmat(1) = 1.
zmat(2) = 6.
zmat(3) = 7.
zmat(4) = 8.
zmat(5) = 19.
zmat(6) = 15.
zmat(7) = 16.
zmat(8) = 20.
```

```
weight(1) = .10200
weight(2) = .18400
weight(3) = .03200
weight(4) = .67700
weight(5) = .00125
weight(6) = .00125
weight(7) = .00125
weight(8) = .00125
```

```
call GSMIXT(46, G_TISSUES', amat, zmat, 1.04, 8, weight)
```

```
C=====
C *** Skin, by weight (From Hammerstein) ***
C=====
```

```
amat(1) = 1.00794      ! H
amat(2) = 12.011      ! C
amat(3) = 14.00674    ! N
amat(4) = 15.9994     ! O
amat(5) = 39.098      ! K
amat(6) = 30.99773762 ! P
amat(7) = 32.068      ! S
amat(8) = 40.078      ! Ca
```

```
zmat(1) = 1.
zmat(2) = 6.
zmat(3) = 7.
zmat(4) = 8.
zmat(5) = 19.
zmat(6) = 15.
zmat(7) = 16.
zmat(8) = 20.
```

```
weight(1) = .09800
weight(2) = .17800
weight(3) = .05000
weight(4) = .66700
weight(5) = .00175
weight(6) = .00175
weight(7) = .00175
weight(8) = .00175
```

```
call GSMIXT(51, 'SKIN$', amat, zmat, 1.09, 8, weight)
```

```
C=====
C *** Neutronium – Hypothetical material with infinite stopping power ***
C=====
```

```
amat(1) = 238.
```

```
zmat(1) = 92.
```

```
weight(1) = 1.
```

```
call GSMIXT(24, 'NEUTRONIUM$', amat, zmat, 200000, -1, weight)
```

Description of the function called to define the material:

Mixtures and compounds are defined using the function GSMIXT: Defines mixture or compound IMATE as composed by NLMAT materials defines via the arrays A, Z, WMAT. Mixtures of compounds can also be defined.

CALL GSMIXT (IMATE, NAMATE, A, Z, DENS, NLMAT, WMAT)

IMATE (INTEGER) user material (mixture) number;

NAMATE (CHARACTER*20) mixture name;

A (REAL) array of atomic weights;

Z (REAL) array of atomic numbers;

DENS (REAL) density in g cm^{-3} ;

NLMAT (INTEGER) number of elements in the mixture;

WMAT **> 0** contains the proportion by weights of each material in the mixture;
< 0 contains the proportion by number of atoms of each kind; the content of WMAT in output is changed to contain the relative weights.

Description of the cone beam angle completely irradiating the breast phantom:

In **USRDET.F** file, the limits for the polar and azimuthal angles are defined and are used in **DIRECTION.F.LIMITED.HD1** FILE.

```
VALPHIMAX = ATAN(SIZE(2)/radius_real)      ! SIZE(2): half the size of the crystal
VALTHETAMAX = ATAN(22./radius_real)       ! radius_real: distance between the
```

DIRECTION.F.LIMITED.HD1 defines the cone beam angle.

```
C define the maximum value for phi and theta
    philimit = VALPHIMAX      ! radian from USRDET.F
    thetalimit = VALTHETAMAX ! radian from USRDET.F

C Set the seed for the first x-ray, for different direction each time we run the simulation
    if (MYEVENT .eq. 1) then
C      seed1 = NRNDM(1)
        seed1 = 20
    end if

    if (MYEVENT .le. 10) then
        write(6,*) 'RANDOM NUMBER =',NRNDM(1),NRNDM(2)
    end if
```


C Pick random numbers for theta and phi

```
do count = 1, 6
```

```
  ran1(count) = ran(seed1)
```

```
end do
```

```
val1 = a90+ran1(1)*thetalimit    ! as the central axis of the cone-beam passes along  
                                the top of the breast phantom
```

```
thetahat = val1
```

```
val1 = ran1(4)*philimit          ! incident on the whole detector
```

```
val2 = a360-ran1(5)*philimit
```

```
if (ran1(6) .lt. .5) then
```

```
  phihat = val1
```

```
else
```

```
  phihat = val2
```

```
end if
```

C Convert from Radians to Degrees

```
theta_degree = thetahat *180./ACOS(-1.)
```

```
phi_degree  = phihat  *180./ACOS(-1.)
```

```
RETURN
```

```
END
```

Appendix E

Operating procedure for DETECT-II simulation [31]

A. Introduction

DETECT-II uses a Monte-Carlo method to simulate the light transport process (simulated emission) in an organic light emitting diode by inputting the photo-luminescence spectra. The advantage of the Monte-Carlo method is that we could keep track of the light scattering process of each individual photon, thus getting the statistically average output spectra in a flexible, accurate, and fast manner.

B. Computational Modeling

The optical scattering process will be affected by *the material properties*, such as refractive index $n(\lambda)$ and absorption coefficient $\mu_{abs}(\lambda)$, *the dimension of the device, the surface types* (flat or rough, partial or perfect reflector, Lambertian diffuse reflector, thin film, etc.), *the source characteristics* (isotropic or Lambertian, point, pencil beam or distributed in a plane, the energy distribution, and the polarization handling). We modify the parameters of the optical scattering process by **Inputs**, run the simulation, and get the results from the **Outputs** described below.

C. Inputs

DETECT-II uses six input files to run a simulation:

1. geometry.in
2. material.in
3. spectrum.in
4. surface.in
5. sensor.in
6. input.in

Each file contains parameters used by DETECT-II for simulation.

D. Outputs

Output files are in the *.out format. Below are three common output files in DETECT-II:

1. case.out
2. 3det.out
3. collect.out

geometry.in

A sample geometry.in file is shown below:

```
Geometry and material description file (preserve format of blank spaces/lines)
***** Overall Dimensions of the object (cm) ***** c.m_m
    10009          10009  100

***** Number of Z slabs *****
1      ORDERED: FROM BOTTOM TO TOP, 1 is BOTTOM, and last is TOP

*****
1
100
2001  2001
P
      2          number of subunits
      9      1    dimensions
      2      1    material
*****
```

It is important to note that the spacing and format of the file must be preserved (DETECTII “looks” for parameters in defined locations in each file).

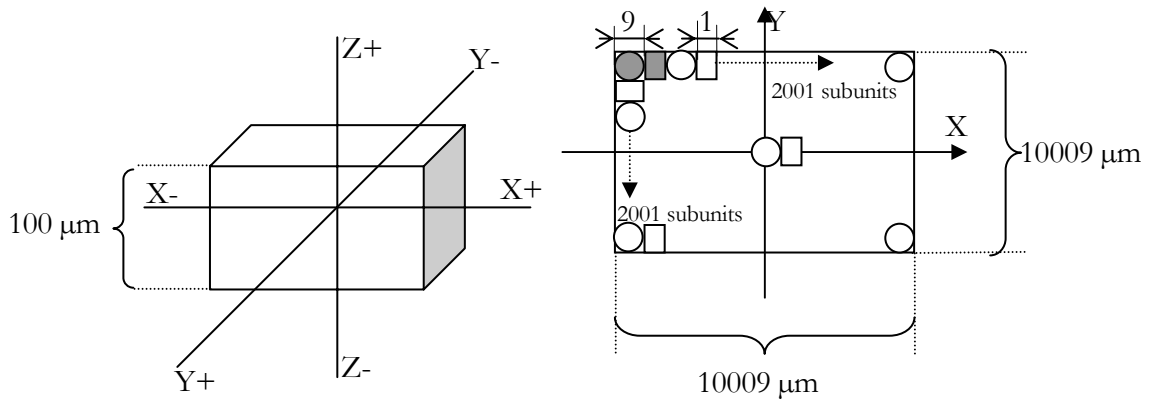
List of “geometry.in” parameters:

- Overall dimensions of the object: **10009 10009 100**
 - This is the size of the entire cubical structure being analyzed (X, Y, Z).
Units are in microns!
- The number of Z-slabs: **1**
 - This is the number of horizontal slabs (or layers) that you want the structure to be divided into the Z-direction

- Information about the individual slabs follows this section.
- Slab number: **1**
 - This is used to identify each particular slab. Slabs are ordered from bottom to top. The first section is always 1, then 2, and so on.
- Slab thickness: **100**
 - This is the thickness (in microns) in the Z-direction of the slab being considered.
- Slab array: **2001 2001**
 - This is to designate which array is being considered. Slabs can be divided into arrays in the X- and Y-directions. These numbers correspond to the number of subunits in the X- and Y-directions respectively.
- Unit description: **P**
 - This is to designate the type of unit of the slab array (P=periodic, F=Uniform block)
- Number of subunits: **2**
 - This is to describe the number of subunits in each unit (CsI + air).
- Dimensions of the subunits: **9 1**
 - This is to describe the dimensions of the units (in microns) by rank (CsI, air)

- Material: 2 1

- This is to describe the material by rank of each subunit as reference in the material.in file (CsI, air)



- Calculation of the different parameters:
 - Unit = 2 subunits of respectively CsI (9 μm) and air (1 μm)
 - Overall dimensions of the object (10000 μm) = 10009 because we want a CsI cylinder in the middle of the detector
 - Dimensions of a unit = 9 + 1 = 10 μm
 - Number of units: $(10009 - 9) / 10 = 1000$
 - Number of subunits = $(1000 \times 2) + 1 = 2001$

material.in

A sample of material.in file:

```
Material description file (preserve format of blank spaces/lines)
!-----
# of materials other than air (air is the zero material)
order is defined as numbers used in the geometry.in file
2
!-----
air.dat
phosphor_csi.dat
OLED_polymer.HTL
OLED_polymer.EL
OLED_substrate_gral
OLED_ito
OLED_glass
OLED_polymer_gral
OLED_polymer.1
OLED_SiO2
OLED_Si3N4
OLED_ito

OLED_polymer.2
```

The material.in describes the materials in the model:

- Number of materials: **2**
 - The number of materials in the model (CsI + air)
- List of Materials
 - List of materials used in the model. The list (top to bottom) corresponds to the material rank in the geometry.in file (which is modeled from bottom to top). In this case, the redefined air material is the first material.
- Default material = air = 0

Note: The material files must be in the same directory where DETECTII is run.

phosphor_csi.dat

A sample of a “material”.dat file:

```
6
5 8 11 13 14 19
.0401 .5396 .0282 .0116 .3772 .0033
2.23
and therefore has modest x-ray attenuation.
This composition was taken from Corning No. 7740

!----- this is line 13 -----
Optical parameters (use same number of digits)
enter first number of wavelength points to use (max. 30)
then, wavelenghts (as integers, in nm)
then, n(wavelenghts)
then, absorption coeff (wavelenghts) (in cm-1)
then, wavelength for the scattering coeff
then, scattering coeff (in cm-1)

1
500  1.8

500  1.0

500
600
T
```

- The first 12 lines should be disregarded. They are not used in our case
- Only the lines after line 13 are interesting for DETECTII
- **1.8** corresponds to the reflective index
- **1.0** corresponds to the absorption coefficient

- **600** corresponds to the scatter coefficient
- The last parameter **T** (true) means that the material is a scintillator and that light is generated. For the air.dat file, this last parameter will be **F** to signifying that no light is generated.

Spectrum.in

A sample of spectrum.in file is shown:

Place spectrum for sampling photon wavelength. First, introduce number of lines to describe the source spectrum at binwave in bwave.

```
&binwave bwave= 17 /
```

Then, enter the wavelength lines used to describe the spectrum in wspect. And the probabilities of emission for these lines.

The sum of all pspect must add to 100.0

```
400 0.05
425 0.15
450 0.28
475 0.45
500 0.73
525 0.95
550 1
575 0.95
600 0.8
625 0.63
650 0.45
675 0.25
700 0.12
725 0.03
750 0
775 0
800 0
```

```
500 1
```

```
400 0.01053
400.5 0.01035
401 0.00995
401.5 0.0095
402 0.00907
```

402.5	0.0093
403	0.00869
403.5	0.00873
404	0.00834
404.5	0.00805
405	0.00802
... <i>And so on...</i>	

The spectrum.in file describes the light source from within the model.

This file is not used because nothing in the material file is wavelength dependent.

Surface.in

An example of surface.in file:

```
Surface description file (preserve format of blank spaces/lines)
!-----
! Number of non-default surfaces (SLABS BOT-TOP: FIRST 6 THEN 3 AUTO)
6
Given as:
! slab#  x#  y#  surface type ordered as 1=xmax,2=ymax,...
1 1 1 6 21 2
1 1 1 3 6 2
1 1 1 4 5 3
1 1 1 5 5 4
1 2001 2001 1 5 4
1 2001 2001 2 5 3

Surface types:
    1 smooth
    2 rough
    3 partially absorber/rough reflector
    4 partially absorber/specular reflector
    5 absolute killer
    6 partially absorber/diffuse reflector
    7 thin film
    8 free pass
    20 detector_plus
    21 detector_minus
    22 detector_BM_plus
    23 detector_BM_minus

Assign the surface type default in the following namelist
&surf surfdefault=1 /

Number of thin films:
&tf tf_number=1 /

Thin film materials and thickness in nm (should be ordered by appearance):
4 200
```

We could input the surface types through this file by modifying given lines.

- Number of non-default surfaces: **6**

- Description of the surfaces: **1 1 1 6 21 2**
 - This first code means the slab number species in the geometry.in file
 - The second and the third codes specify the X and Y positions of the subunit in the array
 - The fourth code specifies the surface (1:X+, 2:Y+, 3:Z+, 4:X-, 5:Y-, 6:Z-), with Z+ at the top and Z- at the bottom
 - The fifth code specifies the surface types
 - The sixth code specifies the array (1:just that all, 2: all row cell, 3: all column cell, 4: all cell in the slab)

- `&surf surdefault=1/`
 - this code specifies which surface we want to make as the default surface (in our case, the smooth surface is the default surface)

sensor.in

A sample of sensor.in is shown below:

```
Place spectrum for sampling photon wavelength. First, introduce
number of lines to describe the source spectrum at binwave in bwave.

&binsensorwave bsensorwave= 17 /

Then, enter the wavelength lines used to describe the spectrum
in wspect. And the probabilities of emission for these lines.
The sum of all pspect must add to 100.0

400 0.503497
425 0.533232
450 0.574042
475 0.645509
500 0.691617
525 0.737725
550 0.765389
575 0.77
580 0.765389
600 0.737725
650 0.645509
675 0.507186
700 0.41497
725 0.184431
750 0.092216
775 0.027665
800 0

500 1

400 0.503497
425 0.533232
450 0.574042
475 0.645509
500 0.691617
525 0.737725
550 0.765389
```

575	0.77
580	0.765389
600	0.737725
650	0.645509
675	0.507186
700	0.41497
725	0.184431
750	0.092216
775	0.027665
800	0

input.in

This file contains parameters in name lists that are often modified during a sequence of runs.

```
This file contains parameters in namelists that are
often modified during a sequence of runs.
!-----
Mcpparameters define the number of histories (pmax) and the maximum
number of events per history (cmax), seed is initial seed for the rng
&mcpparameters pmax_mu=100, pmax_si2=50, cmax=1000, xmax=10000 /
!-----
Sourcetype defines source geometry, source directionality,
source energy and source polarization. The definitions are as follow:
sg=1: point sg=2: planar
sd=1: isotropic in z>0          sd=11: isotropic in z<0 sd=3: full isotropic
sd=2: lambertian z>0 sd=22: lambertian z<0
sd=4: oriented along the z axis (to the semi-plane z>0)(40:z<0)
sd=41: oriented along an arbitrary incident angle (wrt to the normal)
se=1: sampled from a multiple-line table at "spectrum.in"
se=2: uniformly distributed in visible (400-700 nm)
se=3: sampled from function
      blablabla
sp=1: no polarization effect, assuming always averaged equations
      note: handling of Rayleigh scattering without polarization
      is not valid
sp=2: random linearly polarized emission
&sourcetype sg=1, sd=3, se=1, sp=2 /
&expsource expslab=1, expl=1 /
&incidence_angle iangle=45 / this for specular reflectance calculations
&scattering_type scat_type=2 /
!-----
Binangle defines the maximum angle for the tallying
solid angle with respect to the normal, and the restriction
angle for rough reflectors.
&binangle phimax=0, beta=0 /
!-----
Surftypes define percentage of absorption for absdiffuser. (in %)
Test pattern radius (do: external radius, dd: internal radius).
r1 and r2 define a annulus aperture at the top of the model.
&surftypes abssmoothfrac=0, absdifffrac=95, absroughfrac=0, absmirfrac=0, detrefl=10 /
      DATA FROM NISHIKAWA & YAFFE 1990 MEDPHYS 17(5)
&aperture r1=0., r2=0. /
```



```

&spot dd=0., ddo=0. / Note: test pattern is dd=0.195, ddo=1.9
!-----
Densito provides maximum binning radius for densitometer-type binning
at the bottom (2) and up (1) sides
&densito rademerge(1)=0.0,rademerge(2)=0.0 /
!-----
Startposition defines the source location for point sources (%,%,cm)
&startposition ipos(1)=.5, ipos(2)=.5, ipos(3)=.00995 /
!-----
Exposition defines the source location for linear exponential sources (%,%)
&exposition ipos(1)=.5, ipos(2)=.5 /
!-----
Planarposition defines the source location for planar sources
&planarposition iplane=3, ipos(1)=0., ipos(2)=0., ipos(3)=0.1303 /
&planarposition_limits ilimits(1)=0.00, ilimits(2)=0.256,
    ilimits(3)=0.00, ilimits(4)=0.1 /
!-----
Tallying choices with bt (regarding display applications)
bt=1: p(r)/dr/dsr
bt=2: p(r)/dA/dsr
bt=3: p(r)/dA/dsr backprojected (for observer applications)
bt=4: validation of reflective surfaces
bt=5: p(r)/dr/dsr and x,y binning for 3D plots
bt=6: p(r)/dA/dsr and x,y binning backprojected for 3D plots
bt=7: 1+2
bt=8: diffuse reflectance calculation
bt=9: specular reflectance calculation
bt=10: p(r)/dr/dsr and x,y binning for 3D plots with planar detector
Tallying choices with ba (regarding binning of angular distributions)
ba=1: without angular distribution; ba=2: with angular distribution
Tallying choices with be (regarding events statistics)
be=1: without scattering events statistics; be=2: with
Tallying choices with bw (regarding wavelength distributions)
bw=1: without binning of successfull photon wavelength; bw=2: with
Binning of 3d paths
b3d=1: without; b3d=2: with (includes output of 10 files)
if b3d is turned on, will read next lines as entries!

-----
&binningtype bt=10, ba=1, be=1, bw=1, b3d=1, bz=1 /
&collections collect=.T. /

-----
Binning array size for detector runs
&binarraysize xsize=10000, ysize=1 /
&binangle angn=10000 /

```

```
Values of rbin (must be rbin_num consecutive radii from 0)
&pathtype rbin_num=1, path_num=100 /
1
!-----
```

- `cmax` is the maximum number of interactions per event which can occur in order to speed up the simulation
- The parameters that can be adjusted to run a simulation are:
 - The number of histories: given multiplying `xmax` by `pmax_mu`
 - The type of source: **&sourcetype sg=1, sd=3, se=1, sp=2**
 - The type of surface: **&surftypes**
 - **abssmoothfrac=0**
 - **absdifffrac=95** (backing absorption)
 - **absroughfrac=0**
 - **absmirfrac=0**
 - **detrefl=10** (sensor reflectivity)
 - The location of the source
 - The X and Y positions of the source are given as a fraction of the size of the detector: 0.5 = centered point source
 - The Z-position (depth) is in cm from the bottom to the top of the detector

- The size of the binning
 - **&binarray xsize=10000, ysize=1** signifies that 10000 bins will be taken into account in the X-direction and only 1 bin in the Y-direction (sum over Y)

case.out

The case.out file is shown as below. It contains the information of the fraction of the absorption, waveguiding, and the extraction in the specified structure and materials.

Case options:	1	3	1	2
dII statistics:				
bulky absorbed in the structure			375498	
exit by wrong sides			0	
ordered by sides (includes spot binning):				
x+	0			
y+	0			
z+	0			
x-	0			
y-	0			
z-	0			
mean # of photons per interaction			99	
trapped (TF) or killed in surface			624164	
counted		0		
detected		115964		
total number of events		7720859		
total number of scattering events		0		
mean # scatterings per histories		0.0000000E+00		
mean # absorptions per histories		0.3756250		
mean number of events all included		0.0000000E+00		
mean distance per history (cm)		7.4340133E-03		
time/track (seconds)[real-time]		1.6946280E-05		
extraction efficiency [%]		0.0000000E+00		
collection efficiency [%]		11.60032		
lost somewhere (just checking)			0	

- If the last line is not 0, photons had been lost because the number of interactions was greater than cmax (maximum number of interactions allowed)
- X+, Y+, ... etc... should always be 0 which means that nothing went out of the detector
- The time of a simulation is calculated by multiplying the time/track by the total number of events

3det.out

This file gives the number of optical photons per bin in the X-direction for the depth of interaction considered. This allows plotting the Line Spread Function (LSF).

collect.out

This file allows plotting the histogram of the detected photons and calculating the mean value (collection efficiency) and the FWHM.

